

Chandra Observation of NGC 4449. Analysis of the X-ray Emission from a Dwarf Starburst Galaxy.

Lesley K. Summers¹, Ian R. Stevens¹, David K. Strickland^{2*} and Timothy M. Heckman²

¹ School of Physics & Astronomy, University of Birmingham, Edgbaston, Birmingham, B15 2TT, UK

lks@star.sr.bham.ac.uk; irs@star.sr.bham.ac.uk

² Department of Physics & Astronomy, The Johns Hopkins University, 3400 North Charles Street, Baltimore, MD 21218, USA

dks@pha.jhu.edu; heckman@pha.jhu.edu

Accepted; Received; in original form

ABSTRACT

We present *CHANDRA* X-ray data of the nearby Magellanic Irregular dwarf starburst galaxy NGC 4449. Contributions to the X-ray emission come from discrete point sources and extended diffuse emission. The extended emission has a complex morphology with an extent of $\sim 2.4 \times 1.6$ kpc down to a flux density of 1.3×10^{-13} erg s⁻¹ cm⁻² arcmin⁻². The best spectral fit to this emission is obtained with an absorbed, two temperature model giving temperatures for the two gas components of 0.28 ± 0.01 keV and 0.86 ± 0.04 keV, a total mass content of $\sim 10^7 M_\odot$ compared with a galactic mass of several $10^{10} M_\odot$ and a total thermal energy content of $\sim 2.5 \times 10^{55}$ erg, with an average energy injection rate for the galaxy of a few 10^{41} erg s⁻¹. Comparison of the morphology of the diffuse X-ray emission with that of the observed H α emission shows similarities in the two emissions. An expanding super-bubble is suggested by the presence of diffuse X-ray emission within what appears to be a cavity in the H α emission. The kinematics of this bubble suggest an expansion velocity of ~ 220 km s⁻¹ and a mass injection rate of $\sim 0.14 M_\odot$ yr⁻¹, but the presence of NGC 4449's huge HI halo ($r \sim 40$ kpc) may prevent the ejection, into the inter-galactic medium (IGM), of the metal-enriched material and energy it contains.

The arcsecond-resolution of *CHANDRA* has detected 24 X-ray point sources down to a completeness level corresponding to a flux of $\sim 2 \times 10^{-14}$ erg s⁻¹ cm⁻², within the optical extent of NGC 4449 and analysis of their spectra has shown them to be from at least 3 different classes of object. As well as the known SNR in this galaxy, it also harbours several X-ray binaries and super-soft sources. The point source X-ray luminosity function, for the higher luminosity sources, has a slope of ~ -0.51 , comparable to those of other starburst galaxies.

Key words: ISM: jets and outflows – galaxies: individual: NGC 4449 – galaxies: starburst – X-rays: galaxies.

1 INTRODUCTION

NGC 4449 is a nearby Magellanic Dwarf Irregular starburst galaxy which has an inclination of 56.2° and a mass of $\sim 4 \times 10^{10} M_\odot$ (Bajaja et al. 1994 - mass has been scaled for our assumed distance which is discussed later). As such it allows another opportunity for the study of the starburst phenomenon and its effect on galaxy evolution in the local Universe. Dwarf galaxies as the basic building blocks

in the hierarchical merging cosmology scenario are likely to have harboured the earliest sites of star-formation in the Universe and so their study in the local Universe can give insight into the evolution of such objects at high redshift. Observations of local edge-on starburst galaxies (Strickland et al. 2000; Weaver 2001) are presenting a picture of kpc-scale, soft X-ray emitting, bi-polar outflows in the form of galactic winds transporting mass, newly synthesized heavy elements and energy into the IGM. These winds result from the pressure driven outflows along these galaxy's minor axis produced from the efficient thermalization of the mechani-

* *Chandra* Fellow

cal energy from the supernovae (SN) explosions and stellar winds of the massive stars in their OB associations and super star clusters (SSC). Inclined galaxies such as NGC 4449 containing such phenomena present a less clearly observable picture. However, observations of how absorption and temperature of the diffuse X-ray emission varies within them and links between H α , HI and X-ray morphology suggest a similar scenario also applies to these objects.

NGC 4449 has been observed across the electromagnetic spectrum and displays some both interesting and unusual characteristics. Radio observations have shown it to contain an extremely luminous SNR (Bignell & Seaquist 1983), have a very extended HI halo (~ 40 kpc in radius) which appears to be rotating in the opposite direction to the gas in the core of the galaxy (Bajaja et al. 1994) and to have a large-scale ordered magnetic field (Klein et al., 1996). The angular velocity of the rotation of the gas in the centre of the galaxy is low (~ 18 km s $^{-1}$ Hunter et al. 1998), suggesting a low escape velocity but the huge HI halo may prevent escape of the hot ejecta of the starburst region from the galaxy as a whole. The galaxy has both a high star-formation rate (~ 0.2 M $_{\odot}$ yr $^{-1}$, Thronson Jr. et al. 1987) and supernova rate, contains numerous star clusters (~ 60 , Gelatt et al. 2001) with the central one appearing to be young ($\sim 6 - 10$ Myr Böker et al. 2001) and a spherical distribution of older stars with a mean age of 3–5 Gyr (Bothun 1986). It has also been shown to contain molecular cloud complexes from CO observations (Hunter & Thronson Jr. 1996) and has an infra-red luminosity (10 – 150 μ m) of 3.7×10^{42} erg s $^{-1}$ (Thronson Jr. et al. 1987, corrected for the distance assumed here - see below). The ionised gas it contains shows a very disturbed morphology and includes what appear to be many H α bubbles, shells and filaments (Hunter & Gallagher 1990; 1997). The kinematics of the HII regions within the galaxy are very chaotic and could be the aftermath of a collision or merger (Hartmann et al. 1986). There is a gas-rich companion galaxy lying at a projected distance of ~ 40 kpc, coincident in projection with the outer edge of the extended HI halo, which could have been involved. Previous X-ray observations of this galaxy have detected the presence of discrete emission from point sources and diffuse emission from hot gas (Della Ceca et al. 1997; Vogler & Pietsch 1997).

The distance to NGC 4449 is not well established and ranges from 2.93 Mpc (Karachentsev & Drozdovsky 1998) to 5 Mpc (Aaronson & Mould 1983). We have chosen to adopt the lower value throughout this analysis as optical observations are showing objects within NGC 4449 to be resolved (Whiting 2002, private communication) suggesting a lower distance estimate to be more appropriate.

In Section 2 we describe the *CHANDRA* observation. The X-ray emission from the point sources is discussed in Section 3 and that from the diffuse emission is considered in Section 4. Section 5 contains a more general discussion of the relationship of the X-ray emission to that from other wavebands, the affects of the out-flow of the X-ray emission on NGC 4449 and the morphology of the X-ray emission, whilst our main conclusions are summarized in Section 6.

2 OBSERVATIONS AND ANALYSIS

A 30 ks observation of NGC 4449 was obtained on Feb 4th – 5th 2001. Analysis was carried out on the data contained within the S3 chip of the ACIS–S instrument on board *CHANDRA* using *CIAO* (version 2.2.1), *HEASOFT* (version 5.1), *XSPEC* (version 11.1.0) and *ASTERIX* (version 2.3-b1). The data were reprocessed (CALDB version 2.9) and filtered to remove periods of flaring and lower than average count rates using the 3σ clipping technique of the `lc_clean.sl` script (available from the *CHANDRA* website). After these processes were completed, a total of 22.12 ks of useful data remained. The data were then further filtered to contain data in the energy band from 0.3 – 8.0 keV (amounting to a total of ~ 22300 counts on the S3 chip, of which ~ 10700 come from within the D_{25} ellipse and of these ~ 6100 are due to diffuse emission) and were also background subtracted using the appropriately scaled CXC background event data set. (The one utilized for this observation had a total exposure of 137391s.) After production of an exposure map, the point sources present in the data were detected using the *wavdetect* tool, contained in the *CIAO* software, run with an exposure map, default wavlet scales of 2.0 and 4.0 pixels and a source significance threshold of 5×10^{-7} , a value of $\sim (\text{number of pixels})^{-1}$ which should have limited the number of false detections to ~ 1 . 32 point sources were detected and these are shown in Fig. 1 overlaid on a smoothed image of the S3 chip (smoothed with a Gaussian having a FWHM of 4 pixels $\sim 2''$), while their positions and background subtracted count rates are listed in Table 1. Of these 32 sources, 8 do not lie within the optical extent of the galaxy, as measured by the D_{25} ellipse (de Vaucouleurs et al. 1991), also shown in Fig. 1. The 24 sources within the optical extent of the galaxy are the ones most likely to be associated with NGC 4449 and so are the only ones considered further in this analysis. In comparison, when the data were point source searched using *celldetect* with an exposure map and default settings, only 18 sources were detected on the S3 chip. It was obvious from visual inspection of the data that several significant sources were missed by *celldetect*. In addition on comparison with expected source counts from, ‘The *CHANDRA* Deep Field North Survey’ (Brandt et al. 2001), we would expect $\sim 16 - 20$ background sources on the S3-chip at our level of completeness (see section 3.1 for further details). For these reasons, we would expect more than the 18 sources detected by *celldetect* and so the results from *wavdetect* have been adopted as being more reliable.

After detection, the point sources were subtracted from the data so that the diffuse X-ray emission contained within NGC 4449 could be investigated. The sources were simply blanked, using areas equivalent to the 3σ detection ellipses from *wavdetect* and allowance was made for the lost flux from these areas, which amounted to only 0.5% of the total diffuse emission, in later analysis. Also, a 3 colour adaptively smoothed image of the galaxy has been produced using *csmooth* in `fft` (fast fourier transform) mode and this is shown in Fig. 2. The lower and upper sigmas for deriving the smoothing kernel were set at 2 and 5 respectively. This image shows that some of the sources are very soft and that the diffuse emission appears to consist of components of varying temperatures. The red, green and blue images used correspond to energy bands of 0.3 – 0.8 keV, 0.8 – 2.0 keV

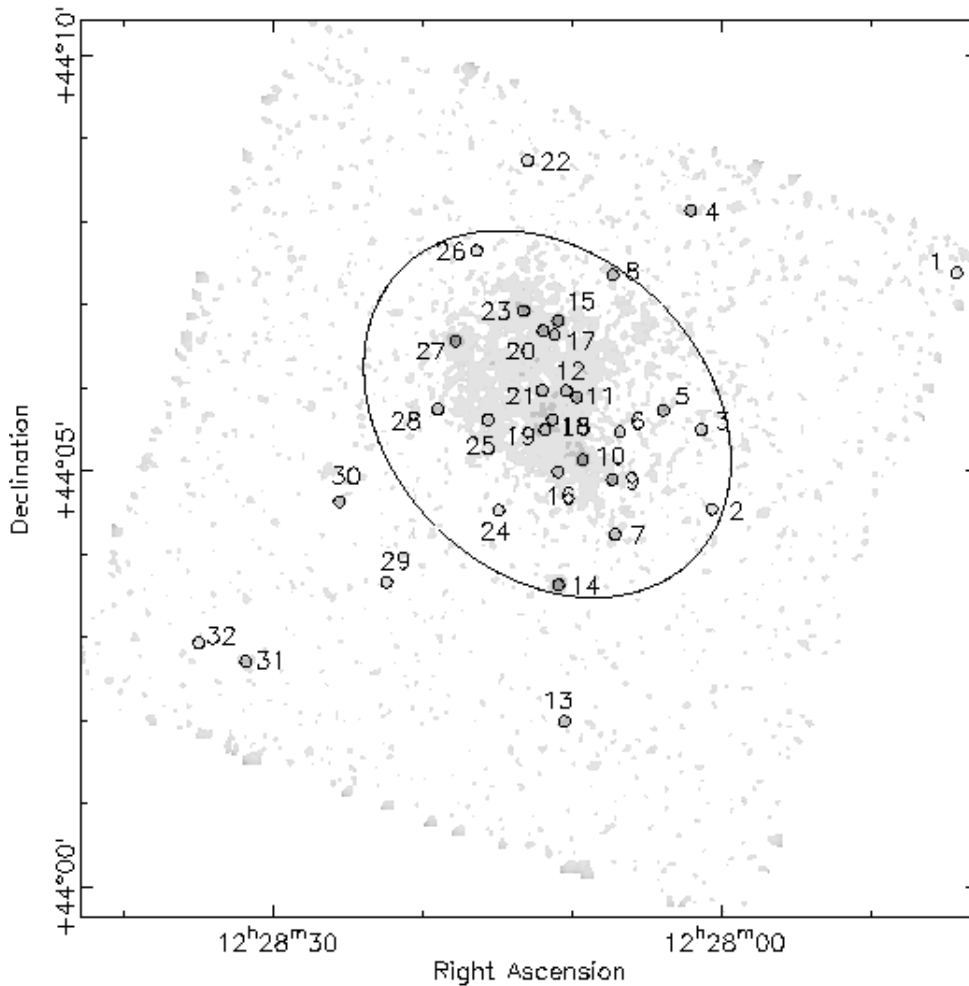


Figure 1. Low resolution (smoothed using a Gaussian with FWHM of 4 pixels $\sim 2''$), background subtracted image of the S3 chip field of view marked with the 32 point sources listed in Table 1 and the D_{25} ellipse, representing the optical extent of NGC 4449. The extended diffuse emission associated with the galaxy is clearly visible.

and 2.0 – 8.0 keV respectively. These bands were chosen so that the total number of counts in each band was approximately equal thereby maximizing the S/N ratio for the 3 bands and allowing point source searching of these individual bands to be performed most effectively. These bands are also in line with those used in the analysis of other starburst galaxies (e.g. NGC 253, Strickland et al. 2002). The diffuse emission is seen to be extended and the size of the region it occupies extends 2.4 kpc from NNE to SSW and 1.6 kpc from WNW to ESE down to a flux density of $1.3 \times 10^{-13} \text{ erg s}^{-1} \text{ cm}^{-2} \text{ arcmin}^{-2}$.

The background subtracted spectrum of the total X-ray emission from within the D_{25} ellipse of NGC 4449 was fitted using the modified Levenberg-Marquardt method and standard χ^2 statistic from *XSPEC*, with an absorbed 2 thermal component plus power law fit. The resulting spectral fit is shown in Fig. 3. The absorbing column density was considered to be two components, one due to the interstellar medium (ISM) within the Milky Way (Galactic column density, $N_H = 1.4 \times 10^{20} \text{ cm}^{-2}$) and the other due to the ISM of NGC 4449. The 2 absorbed thermal components were modelled using the *wabs* (photo-electric absorption using Wisconsin cross-sections) and *mekal* thermal

plasma codes within *XSPEC*, initially Galactic absorption and an abundance of 0.276 Solar (the value obtained by Martin, 1997, for NGC 4449) were assumed. Two thermal plasmas were used to represent the diffuse fraction of the total X-ray emission as images in the soft (0.3 – 0.8 keV) and medium (0.8 – 2.0 keV) energy bands, see Fig. 9, show different spatial distributions of the hot gas and also, multi-phase models are seen to be needed to best fit the emission from other starburst galaxies (e.g. NGC 253, Strickland et al. 2002; NGC 1569, Martin et al. 2002). A single temperature fit to NGC 4449 also gave a less robust statistical fit and in particular when fitted to just the diffuse emission does not have a wide enough energy distribution to fit the spread seen in the data. The two-temperature model gives an absorption corrected flux of $(2.39 \pm_{0.19}^{0.18}) \times 10^{-12} \text{ erg s}^{-1} \text{ cm}^{-2}$, which corresponds to a total X-ray luminosity, in the 0.3 – 8.0 keV band, of $(2.46 \pm_{0.20}^{0.19}) \times 10^{39} \text{ erg s}^{-1}$. The fitted column density for NGC 4449 was $(1.31 \pm 0.52) \times 10^{21} \text{ cm}^{-2}$, with the two thermal components having temperatures of $0.27 \pm 0.01 \text{ keV}$ and $1.01 \pm 0.06 \text{ keV}$ and a fitted abundance of $0.29 \pm_{0.08}^{0.54} Z_{\odot}$. The power law component had a fitted photon index of $\Gamma = 2.05 \pm 0.46$. Of this total emission, $\sim 60\%$ is from the

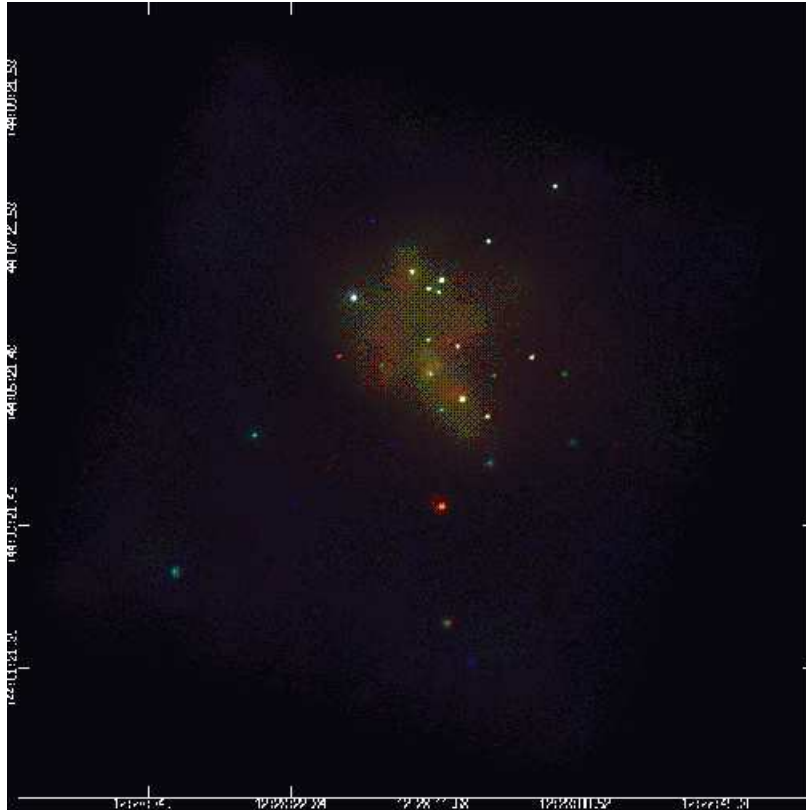


Figure 2. Adaptively smoothed 3 colour image of NGC 4449 (red: 0.3 – 0.8 keV, green: 0.8 – 2.0 keV and blue: 2.0 – 8.0 keV). The extent of the diffuse emission is ~ 2.4 kpc from NNE to SSW and ~ 1.6 kpc from WNW to ESE. The variation of hardness in the spectra of the resolved sources is evident from their varying colours and is indicative of the presence of different types of sources, such as XRBs, SNRs and SSS.

resolved point sources, $\sim 30\%$ is from the cooler thermal component and $\sim 10\%$ is from the hotter component.

3 POINT SOURCES

3.1 Source Spectra

A background subtracted spectrum was extracted for each of the 24 sources within the D_{25} ellipse. (The background spectra were taken from the aforementioned background file and were appropriately scaled. The use of the background files meant that the background spectrum was taken from the identical position on the CCD and avoided the problem of contamination from adjacent sources.) The spectra were grouped so that each had a minimum of 5 data bins and when possible a minimum of 10 counts per bin. No attempt was made initially to fit the data where a source had less than 50 counts after background subtraction. The fits obtained for the 5 sources with the highest count rates are shown in Fig.4. Comparison of the low count spectra to those fitted allowed a rough fit to be made to these sources individually by using the models of sources with similar spectra and hardness ratios (see below). The best fits obtained for the sources are summarized in Table 2. The same start parameters were assumed for column densities and abundances as were used for fitting the total emission.

For each of the individual source fits, the unabsorbed

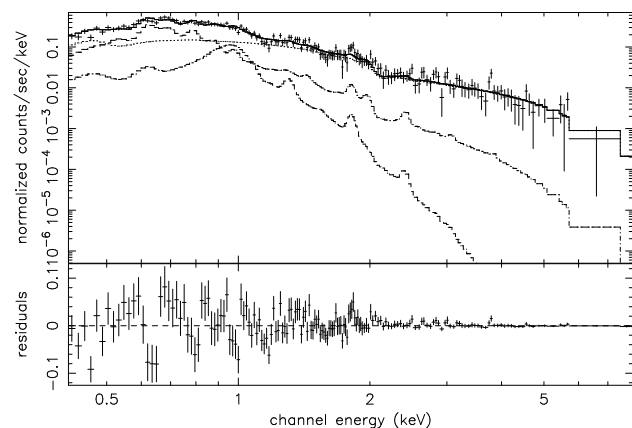


Figure 3. Fitted spectrum of the total X-ray emission from NGC 4449. The fit shown is an absorbed two temperature plus power law fit, with a column density of $N_H = 1.40 \times 10^{20} \text{ cm}^{-2}$ assumed for Galactic absorption and a fitted column density of $N_H = (1.31 \pm 0.52) \times 10^{21} \text{ cm}^{-2}$ for the absorption within NGC 4449. The fitted temperatures of the two thermal components are 0.27 ± 0.01 and 1.01 ± 0.06 keV with the fitted abundance for both components being $(0.29 \pm_{0.08}^{0.54} Z_\odot)$ and the fitted photon index of the power law component having a value of $\Gamma = 2.05 \pm 0.46$. The individual contributions of the separate components of the fit are also included.

Table 1. Positions and count rates of the 32 sources detected in the NGC 4449 *CHANDRA* S3 chip data. Column 1 is the source number ordered in increasing R.A.. Columns 2 and 3 give the R.A. and Dec. of each source and Column 4 lists their background subtracted count rates.

Source	RA (h m s)	Dec ($^{\circ}$ ' ")	Count Rate ($\times 10^{-3}$ cts s^{-1})
1	12 27 44.24	44 07 23.0	0.13 ± 0.08
2	12 28 00.65	44 04 32.5	0.37 ± 0.14
3	12 28 01.36	44 05 29.9	0.63 ± 0.18
4	12 28 02.07	44 08 08.0	5.09 ± 0.48
5	12 28 03.89	44 05 43.8	5.36 ± 0.50
6	12 28 06.82	44 05 28.4	0.83 ± 0.21
7	12 28 07.13	44 04 14.4	0.96 ± 0.22
8	12 28 07.29	44 07 21.6	2.96 ± 0.37
9	12 28 07.34	44 04 53.8	5.65 ± 0.52
10	12 28 09.32	44 05 08.3	43.18 ± 1.42
11	12 28 09.71	44 05 53.1	7.53 ± 0.59
12	12 28 10.40	44 05 58.1	1.96 ± 0.32
13	12 28 10.52	44 01 59.5	1.04 ± 0.24
14	12 28 10.93	44 03 38.0	15.82 ± 0.87
15	12 28 10.95	44 06 48.5	38.60 ± 1.33
16	12 28 10.97	44 04 59.5	0.94 ± 0.23
17	12 28 11.20	44 06 38.5	4.13 ± 0.44
18	12 28 11.33	44 05 37.0	0.50 ± 0.19
19	12 28 11.84	44 05 30.0	1.80 ± 0.32
20	12 28 11.98	44 06 41.5	6.50 ± 0.56
21	12 28 12.02	44 05 58.4	2.18 ± 0.33
22	12 28 13.00	44 08 44.1	0.35 ± 0.13
23	12 28 13.26	44 06 55.8	9.61 ± 0.68
24	12 28 14.93	44 04 31.8	0.36 ± 0.14
25	12 28 15.64	44 05 37.1	0.63 ± 0.19
26	12 28 16.41	44 07 39.1	0.42 ± 0.14
27	12 28 17.83	44 06 33.9	51.35 ± 1.55
28	12 28 19.02	44 05 44.6	1.69 ± 0.28
29	12 28 22.44	44 03 39.7	0.39 ± 0.14
30	12 28 25.60	44 04 37.9	1.41 ± 0.26
31	12 28 31.86	44 02 42.5	1.74 ± 0.33
32	12 28 35.02	44 02 56.0	0.26 ± 0.12

flux in the 0.3–8.0 keV energy band and luminosity (assuming a distance of 2.93 Mpc for NGC 4449) were calculated and these luminosities are also shown in Table 2 along with the errors determined from the 90% confidence regions for each model’s normalization. In addition the data was point source searched in the three different energy bands used to produce the three colour image, (soft 0.3–0.8 keV, medium 0.8–2.0 keV and hard 2.0–8.0 keV) so that hardness ratios for the individual sources within the D_{25} ellipse could be calculated for the sources detected in more than one of the energy bands. These ratios are shown in Table 3. The cumulative $\text{Log}(N)$ – $\text{Log}(L_X)$ plot for the 24 fitted sources possibly associated with NGC 4449 is shown in Fig. 5. This has been fitted with a single power law with a slope of ~ -0.51 for the higher luminosity sources. The highest luminosity source is not included in the fit. To do so results in an offset between the data and the fitted line but does not alter the slope of the fit. The spectral fit to this source (source 28) does suggest it is a very unusual source as it is very soft, lies behind a high column density and has an extremely high luminosity ($> 10^{41}$ erg s^{-1}). The fact that its spectrum contains < 40 counts in total brings into question the robustness of

the fit and for these reasons it has been excluded from the fit. Sources with luminosities below an absorption corrected luminosity of 2.18×10^{37} erg s^{-1} , equivalent to a flux of 2.12×10^{-14} erg s^{-1} cm^{-2} , were also not included in the fit and these figures represent the completeness limit for the data. The fitted value for the slope is comparable to the same fits for M82 and the Antennae where the slope was determined to be $\sim -0.45 \pm 0.06$ (Zezas et al. 2001). The absorption corrected contribution to the X-ray luminosity of NGC 4449 from unresolved point sources is estimated to be $\sim (5.62 \pm_{4.30}^{6.08}) \times 10^{37}$ erg s^{-1} , equivalent to $\sim 5\%$ of the diffuse emission (see section 4).

Earlier *ROSAT* HRI observations of this galaxy (Vogler & Pietsch 1997) detected only 7 point sources within the D_{25} ellipse. Of these 7, at least 3 of them have been resolved into more than one source using the superior arcsecond spatial resolution of *CHANDRA* and an additional 13 sources have also been detected. The source identified as the supernova remnant (SNR), (X4) in the *ROSAT* data corresponds to source 15 in our *CHANDRA* data when the source position is compared to the accurate position for the SNR obtained by Bignell & Seaquist (1983), from radio measurements and there are also 2 additional sources resolved at the position of X4 in the *ROSAT* data. This highlights the fact that luminosity estimates based on pre-*CHANDRA* data are effected by source confusion. Also of note is the fact that source 27 in our data (X7 in the *ROSAT* data) is much more luminous than it was in 1994 and now has the highest count-rate for a single source in the galaxy rather than being fourth highest. See Table 4 for a comparison of the 0.1–2.4 keV absorption corrected luminosities of sources that were both detected by *ROSAT* and not resolved into more than one source by *CHANDRA*.

In general, the sources seem to split into four classes which can be represented by sources 14, 15, 27 and 2. Sources like source 14 are very soft, luminous sources (super-soft sources, SSS) which show little emission above 1 keV. Source 15 is the SNR and at least 5 other sources show similar spectra and/or hardness ratios. Sources like source 2 have spectra that contain hard emission up to ~ 5 keV and sources in this group seem to be best fitted by power law models. They are generally fitted with a higher column density and lower photon index than other sources and may be background AGN. Sources like source 27 also have harder components to their spectra, showing emission above 5 keV and are fitted by power laws with $1.3 \leq \Gamma \leq 3.0$, typical of X-ray binaries (XRB). See Section 3.2 below for further discussion on the brightest sources. Fig. 6 shows a comparison of the hard and soft hardness ratios for the sources detected in all 3 energy bands. The hard ratio is $(h - m)/(h + m)$ while the soft ratio is $(m - s)/(m + s)$, where s is the count rate in the soft band (0.3–0.8 keV), m is the count rate in the medium band (0.8–2.0 keV) and h is the count rate in the hard band (2.0–8.0 keV). The sources represented by squares were only detected in 2 of the 3 energy bands and so their positions represent the most extreme positions possible for them on this plot. Those at the bottom need to move vertically upwards while those to the right will need to move horizontally to the left. The sources appear to clump in groups on this plot with the SNR and SSS sources being softer than those we have classified as XRB and AGN. The right hand plot in this figure shows some theoretical tracks of

Table 2. Best fitting single component models for the spectra of the 24 point sources. Column 1 gives the source numbers as shown on Fig. 1. Column 2 contains the best fit absorbed single component models obtained. In each case, the absorbing column due to the Milky Way, $wabs_{Gal}$ is assumed to be $N_H = 1.4 \times 10^{20} \text{ cm}^{-2}$. Column 3 is the column density obtained from fitting the $wabs$ (photo-electric absorption using Wisconsin cross-sections) component, column 4 the fitted temperature for the mekal, brems (thermal bremsstrahlung), bb (black body), and nei (non-equilibrium ionization) models for the thermal components, column 5 is the photon index for the po (power law) models, column 6 the statistic of each fit and column 7 the absorption corrected luminosity for each source. The errors shown on the luminosities are from the 90% confidence regions (1.64σ) for each model's normalization. Where only one value is shown this is an upper limit from the same 90% confidence regions. Column 8 lists the type of source each object might be from comparison with the spectra and hardness ratios of the identified sources within the galaxy.

Source	Model	N_H (cm^{-2})	kT (keV)	Γ	χ^2 /d.o.f	Luminosity (erg s^{-1})	Source Type
2	$wabs_{Gal}(wabs(po))$	3.14×10^{21}		0.61	1.78/5	$(7.10 \pm^{7.31}) \times 10^{36}$	AGN
3	$wabs_{Gal}(wabs(mekal))$	3.68×10^{21}	0.90		0.49/2	$(5.87 \pm^{2.86}_{0.87}) \times 10^{36}$	SNR/XRB
5	$wabs_{Gal}(wabs(po))$	6.58×10^{20}		1.30	1.39/8	$(5.15 \pm^{0.75}_{0.92}) \times 10^{37}$	XRB
6	$wabs_{Gal}(wabs(mekal))$	1.31×10^{21}	0.82		2.01/2	$(5.51 \pm^{3.52}) \times 10^{36}$	SNR/XRB
7	$wabs_{Gal}(wabs(po))$	1.39×10^{21}		0.40	1.00/2	$(2.18 \pm^{0.98}) \times 10^{37}$	AGN
8	$wabs_{Gal}(wabs(po))$	1.53×10^{20}		1.33	0.38/3	$(2.59 \pm^{2.14}_{0.69}) \times 10^{37}$	XRB
9	$wabs_{Gal}(wabs(po))$	3.93×10^{20}		2.88	7.87/8	$(2.94 \pm^{0.66}_{0.56}) \times 10^{37}$	SNR/XRB
10	$wabs_{Gal}(wabs(brems))$	9.29×10^{20}	1.42		83.37/69	$(2.24 \pm^{0.12}_{0.12}) \times 10^{38}$	SNR/XRB
11	$wabs_{Gal}(wabs(po))$	3.50×10^{21}		1.64	9.07/13	$(8.91 \pm^{1.23}_{1.24}) \times 10^{37}$	XRB
12	$wabs_{Gal}(wabs(bb))$	4.15×10^{20}	0.091		4.46/4	$(1.28 \pm^{2.11}) \times 10^{37}$	SSS
14	$wabs_{Gal}(wabs(bb))$	8.96×10^{20}	0.097		12.44/20	$(1.24 \pm^{0.12}_{0.11}) \times 10^{38}$	SSS
15	$wabs_{Gal}(wabs(nei))$	1.26×10^{21}	2.58		65.50/60	$(2.34 \pm^{0.14}_{0.13}) \times 10^{38}$	SNR
16	$wabs_{Gal}(wabs(po))$	1.40×10^{22}		2.53	0.90/3	$(3.14 \pm^{1.16}_{1.23}) \times 10^{37}$	XRB
17	$wabs_{Gal}(wabs(nei))$	7.45×10^{20}	19.21		5.33/5	$(2.51 \pm^{0.50}_{0.49}) \times 10^{37}$	SNR/XRB
18	$wabs_{Gal}(wabs(nei))$	3.82×10^{20}	3.05		1.03/3	$(3.02 \pm^{1.37}) \times 10^{36}$	SNR/XRB
19	$wabs_{Gal}(wabs(po))$	1.31×10^{21}		1.35	0.47/3	$(2.33 \pm^{1.55}_{0.71}) \times 10^{37}$	XRB
20	$wabs_{Gal}(wabs(po))$	3.45×10^{21}		2.76	8.20/10	$(7.43 \pm^{1.04}_{1.23}) \times 10^{37}$	SNR
21	$wabs_{Gal}(wabs(bb))$	2.45×10^{21}	0.080		1.71/2	$(7.19 \pm^{1.07}_{2.76}) \times 10^{37}$	SNR/SSS
23	$wabs_{Gal}(wabs(nei))$	9.00×10^{21}	1.30		12.07/16	$(8.06 \pm^{0.98}_{1.01}) \times 10^{38}$	SNR/XRB
24	$wabs_{Gal}(wabs(po))$	1.10×10^{22}		0.97	2.25/6	$(5.79 \pm^{5.22}) \times 10^{36}$	AGN
25	$wabs_{Gal}(wabs(bb))$	1.11×10^{21}	0.130		0.62/2	$(5.17 \pm^{107.71}) \times 10^{36}$	SSS/XRB
26	$wabs_{Gal}(wabs(brems))$	4.72×10^{21}	54.85		0.74/2	$(4.99 \pm^{3.57}) \times 10^{36}$	AGN
27	$wabs_{Gal}(wabs(po))$	6.49×10^{21}		1.91	64.38/86	$(8.19 \pm^{0.42}_{0.41}) \times 10^{38}$	XRB
28	$wabs_{Gal}(wabs(bb))$	5.01×10^{21}	0.050		1.28/3	$(4.27 \pm^{1.32}_{1.34}) \times 10^{41}$	SSS

how a sources position would vary depending on which type of spectral model is assumed for it, what value the absorbing column density that it lies behind has and what temperature or photon index is assumed for the model, for comparison with the plotted source positions. An attempt has been made to classify the sources using the shape and range of spectra and their positions on the hardness ratio plot. The suggested classifications are shown in column 8 of Table 2. The D_{25} ellipse covers $\sim 25\%$ of the S3-chip and as such it would be expected from the background number counts quoted in section 2 that $\sim 4 - 5$ background sources should be found within this area. This figure agrees well with the number of sources classified as potential background AGN. In contrast to this, the 8 point sources detected outside the D_{25} ellipse are only about a half to two-thirds of what would be expected, suggesting that our completeness level estimate may be at slightly too low a flux.

3.2 More Detail on the Brightest Sources

3.2.1 Source 10 – SNR?

This source lies in the soft region of the hardness plot of Fig. 6 to the left of the area occupied by the known SNR. It is best fitted by an absorbed thermal Bremsstrahlung model. Its position would also suggest it should have a low column density as it lies to the left of the theoretical tracks. This

does not appear to be the case and fitting with other models gives an even higher column density for a power law model or unphysical results. This source was also detected (source X7) in the earlier *ROSAT* observations and shows no evidence for variability as seen in Table 4. Hence, it seems more likely that it is a SNR than an XRB.

3.2.2 Source 14 – SSS

This source is very soft and it can be fitted in a similar way to CAL 87 (Ebisawa et al. 2001) using an absorbed blackbody component and several absorption edges, indicative of a white dwarf binary system. For such a fit, three absorption edges are included at energies of 0.40 keV, 0.59 keV and 0.85 keV the value of N_H increases to $3.24 \times 10^{21} \text{ cm}^{-2}$ and kT decreases to 0.065 keV, compared to the one component fit shown in Table 2, while the absorption corrected luminosity in the 0.3 – 8.0 keV band increases to $\sim 4.05 \times 10^{39} \text{ erg s}^{-1}$. The absorption edges are possibly connected with the presence of the following elements: 0.40 keV, NVI or CVI; 0.59 keV, OVII or NVII; 0.85 keV, OVIII and/or OVII (the low source counts making a definite identification difficult). The blackbody temperature fitted here lies in the range ($T \sim 60 - 80 \text{ eV}$) where both OVII and OVIII edges would be expected to be present with the latter being more abundant (Ebisawa et al. 2001). This

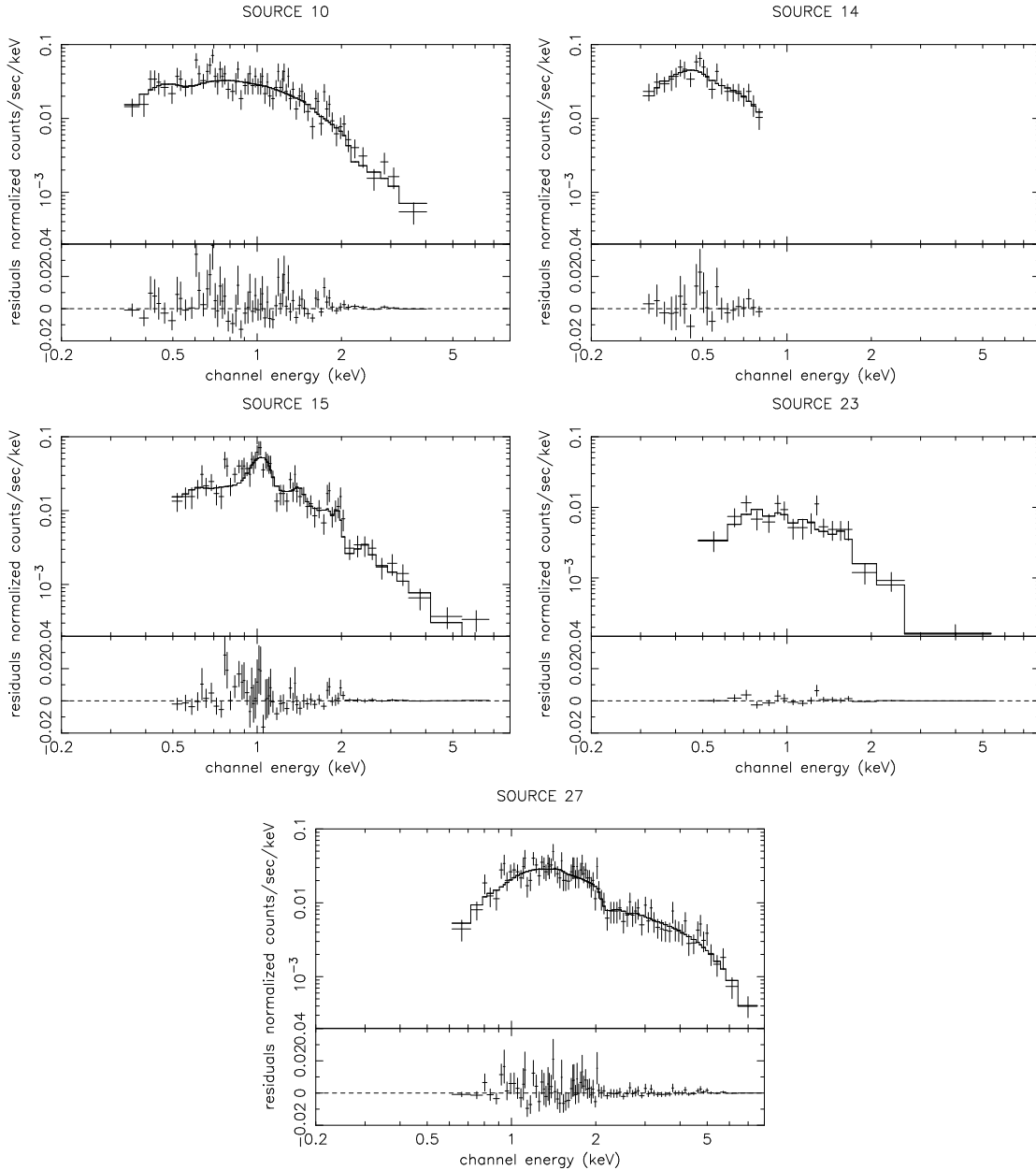


Figure 4. Spectra and best fitting models for the brightest sources detected within the D_{25} ellipse. Results are shown for source 10 (top left), source 14 (top right), source 15 (middle left), source 23 (middle right) and source 27 (bottom). All the fits are for the absorbed one component models shown in Table 2. More detailed fits for the brighter sources are discussed in Section 3.2 of the text.

source has a greatly increased absorption corrected luminosity compared with the earlier *ROSAT* observations however the difference is in part due to the different spectral models used to fit the spectrum. The improved spectral resolution of *CHANDRA* compared with *ROSAT* clearly shows that a 5 keV thermal bremsstrahlung model is inappropriate for this source, as all its emission lies below 1 keV. In Table 4, the absorption corrected luminosity is also much higher than that shown in Table 2 and quoted above due to the value in Table 4 including emission down to 0.1 keV rather than 0.3 keV. These facts make it difficult to assess if there has been any intrinsic increase in the sources luminosity over the last decade. When the *CHANDRA* data are fitted with

the 5 keV thermal Bremsstrahlung model there is agreement with the *ROSAT* HRI data, within errors.

3.2.3 Source 15 – SNR

This source has been identified as a young and very luminous SNR embedded in an HII region from observations in several different wavebands, radio (Seaquist & Bignell 1978), optical (Balick & Heckman 1978, Blair et al. 1983), UV (Blair et al. 1984) and X-ray (Blair et al. 1983; Vogler & Pietsch 1997). Fitting this source with an absorbed, non-equilibrium ionization model (as used for modelling other SNR, e.g. Yokogawa et al., 2002) gives an X-ray temper-

Table 3. Hardness ratios, where possible, for the 24 sources detected within the D_{25} ellipse. Soft band, s , 0.3 – 0.8 keV, medium band, m , 0.8 – 2.0 keV and hard band, h , 2.0 – 8.0 keV. Where no counts are shown, *wavdetect* failed to detect the object in that energy band. Column 1 gives the source numbers as shown on Fig. 1. Columns 2 – 4 are the counts in the 3 different energy bands and columns 5 and 6 give the values of the hardness ratios calculated as detailed in the column headings.

Source	Counts in Soft Band	Counts in Medium Band	Counts in Hard Band	$\frac{(m - s)}{(m + s)}$	$\frac{(h - m)}{(h + m)}$
2	-	2.0 ± 1.4	3.9 ± 2.0	-	0.32 ± 0.43
3	-	8.9 ± 8.0	-	-	-
5	25.7 ± 5.1	58.7 ± 7.7	34.7 ± 5.9	0.39 ± 0.12	-0.26 ± 0.11
6	-	8.9 ± 8.0	-	-	-
7	-	3.9 ± 2.0	7.9 ± 2.8	-	0.34 ± 0.31
8	12.8 ± 3.6	31.8 ± 5.7	20.8 ± 4.6	0.43 ± 0.17	-0.21 ± 0.14
9	55.2 ± 7.5	57.4 ± 7.6	6.9 ± 2.6	0.02 ± 0.10	-0.79 ± 0.16
10	533.7 ± 23.2	336.9 ± 18.4	93.6 ± 10.0	-0.23 ± 0.03	-0.57 ± 0.06
11	23.9 ± 5.0	88.0 ± 9.4	54.6 ± 7.4	0.57 ± 0.11	-0.23 ± 0.09
12	39.6 ± 6.4	-	-	-	-
14	349.0 ± 18.7	7.9 ± 2.8	-	-0.96 ± 0.07	-
15	141.7 ± 12.0	590.5 ± 24.4	126.5 ± 11.3	0.61 ± 0.04	-0.64 ± 0.11
16	-	10.5 ± 3.3	6.9 ± 2.6	-	-0.21 ± 0.17
17	30.1 ± 5.6	54.1 ± 7.4	-	0.29 ± 0.49	-
18	-	-	-	-	-
19	-	22.4 ± 4.9	14.7 ± 3.9	-	-0.21 ± 0.17
20	30.1 ± 5.6	91.1 ± 9.6	19.7 ± 4.5	0.50 ± 0.10	-0.64 ± 0.11
21	14.8 ± 4.0	31.7 ± 5.7	-	0.36 ± 0.16	-
23	51.8 ± 7.3	129.6 ± 11.4	27.6 ± 5.3	0.43 ± 0.09	-0.65 ± 0.09
24	-	-	4.9 ± 2.2	-	-
25	-	-	-	-	-
26	-	-	4.9 ± 2.2	-	-
27	32.4 ± 5.7	669.5 ± 25.9	448.7 ± 21.2	0.91 ± 0.05	-0.20 ± 0.03
28	36.6 ± 6.1	-	-	-	-

Table 4. Comparison of the absorption corrected luminosities for sources 10, 14, 23 and 27 obtained from *ROSAT* PSPC observations (11/1991), *ROSAT* HRI observations (12/1994) and *CHANDRA* ACIS-S observations (02/2001). The *ROSAT* values are from Vogler & Pietsch (1997) and are for 5 keV thermal bremsstrahlung spectra, corrected for Galactic absorption. The first column of *CHANDRA* values are for the best fits discussed in the text, corrected for Galactic absorption. All luminosities are for the 0.1 – 2.4 keV energy band and the *CHANDRA* values have been scaled to account for the differences in assumed distances to NGC 4449. The errors shown on the *CHANDRA* data are from the 90% confidence levels (1.64σ) of the normalizations of the fits. Columns 1 and 2 are the source numbers allocated in the respective data sets and columns 3 – 5 give the absorption corrected luminosities fitted to the 3 data sets. Column 6 shows the absorption corrected luminosities obtained for the *CHANDRA* data when they are fitted with a 5 keV thermal bremsstrahlung model, corrected for Galactic absorption.

Chandra	ROSAT	L_X (PSPC) ($\times 10^{38}$ erg s $^{-1}$)	L_X (HRI) ($\times 10^{38}$ erg s $^{-1}$)	L_X (ACIS-S) ($\times 10^{38}$ erg s $^{-1}$)	L_X (ACIS-S 5 keV) ($\times 10^{38}$ erg s $^{-1}$)
10	X1	2.92 ± 0.43	3.10 ± 0.37	$3.24^{+0.18}_{-0.18}$	$2.58^{+0.15}_{-0.15}$
14	X3	0.70 ± 0.23	1.67 ± 0.27	$105.45^{+9.53}_{-10.18}$	$1.82^{+0.20}_{-0.21}$
23	X6	0.84 ± 0.28	0.76 ± 0.21	$14.60^{+1.87}_{-1.68}$	$1.01^{+0.12}_{-0.13}$
27	X7	1.88 ± 0.37	1.00 ± 0.21	$7.33^{+0.38}_{-0.36}$	$6.18^{+0.33}_{-0.33}$

ature, $T_X \sim 2.2 \times 10^7$ K, a column density of $N_H = 1.26 \times 10^{21}$ cm $^{-2}$ and an absorption corrected luminosity of $L_X = (2.34^{+0.14}_{-0.13}) \times 10^{38}$ erg s $^{-1}$ in the 0.3 – 8.0 keV energy band, which are comparable to the values recently obtained for the same SNR by Patnaude & Fesen (2003). (After allowing for differences in assumed distance, they quote a luminosity of $L_X = 1.4 \times 10^{38}$ erg s $^{-1}$ in the 0.5 – 2.1 keV energy band, a temperature of $T \sim 9.2 \times 10^6$ K and an absorbing column density of $N_H = 1.7 \times 10^{21}$ cm $^{-2}$.) Following the same analysis that Blair et al. (1983) performed on this SNR, we find firstly that our fitted temperature, is higher than the 6×10^6 K assumed by Blair et al. (1983, which

came from the average temperature determined from *Einstein* SSS observations of young SNR). This higher temperature leads to an age for the SNR of ~ 270 yr and a density of $120 - 200$ cm $^{-3}$ for the medium into which the SN exploded. These results are higher than the age of ~ 120 yr and density of ~ 25 cm $^{-3}$ reported by Blair et al. (1983). Allowing for the difference in assumed distances to NGC 4449 would increase our age estimate to ~ 380 yr without effecting the density. Compared to the non-equilibrium ionization fit for the ionization timescale, where $\tau = nt = 4.96 \times 10^{11}$ cm $^{-3}$ s, with the 90% confidence regions for this parameter giving a range of $3.61 \times 10^{11} \leq \tau \leq 5.00 \times 10^{13}$ cm $^{-3}$ s, the product of our

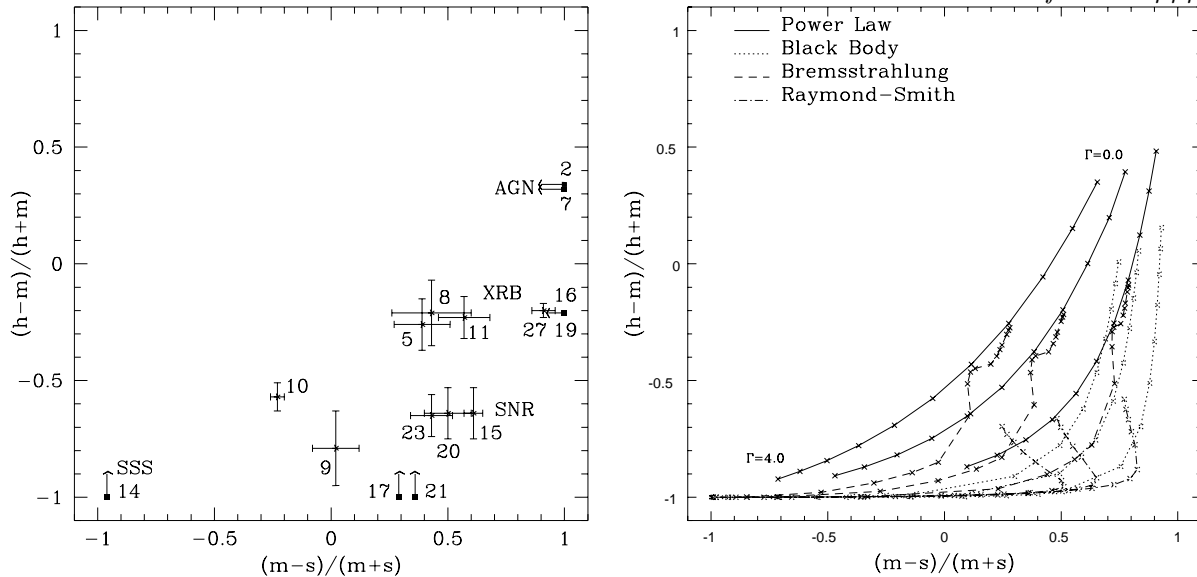


Figure 6. Left: Hard v. soft hardness ratios for the sources detected in the separate energy bands. The hard hardness ratio is calculated from the 2.0 – 8.0 keV and 0.8 – 2.0 keV energy bands and the soft hardness ratio is calculated from the 0.8 – 2.0 keV and 0.3 – 0.8 keV energy bands in the usual way as defined in the headings of columns 5 and 6 of Table 3. An indication of the likely origin of the sources depending on the location in this plot is also shown by the labels placed next to known sources. Right: Theoretical tracks showing the positions different sources would occupy on the hardness ratio plot. The three lines of each type have column densities of $1.4 \times 10^{20} \text{ cm}^{-2}$ (Galactic N_H), $1.0 \times 10^{21} \text{ cm}^{-2}$ (fitted column density for the total emission from NGC 4449) and $3.0 \times 10^{21} \text{ cm}^{-2}$ (average fitted column density for the fitted sources on the hardness ratio plot) respectively, moving from left to right across the plot. For the three thermal models, the temperatures increase from bottom left to top right. Black Body, kT ranges from 0.04 – 1.0 keV; Bremsstrahlung, kT ranges from 0.2 – 100 keV; Raymond-Smith, kT ranges from 0.1 – 2.0 keV and the plots shown are for Solar abundance. Decreasing the abundance moves the Raymond-Smith tracks to the left.

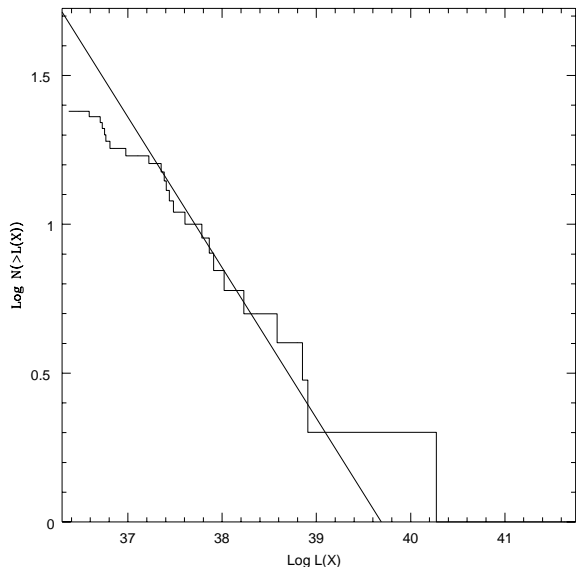


Figure 5. $\log(N) - \log(L_X)$ plot for the 24 fitted resolved point sources lying within the D_{25} ellipse. The line shown is the power law fit to the high luminosity end of the data. The slope of this fit is -0.51 and incompleteness occurs at an absorption corrected luminosity of $2.18 \times 10^{37} \text{ erg s}^{-1}$, which corresponds to a limiting absorption corrected flux of $2.12 \times 10^{-14} \text{ ergs}^{-1} \text{ cm}^{-2}$.

calculated values gives $1.0 \times 10^{12} \leq \tau \leq 1.7 \times 10^{12} \text{ cm}^{-3} \text{ s}$, which gives reasonable agreement for the two methods.

3.2.4 Source 23 – XRB?

The position of this source on the hardness plot of Fig. 6 places it in the group of XRBs however, its spectrum is best fitted by an absorbed non-equilibrium ionization model and this source shows no strong evidence for variability over the past 10 years, factors which may be more indicative of a SNR than XRB.

3.2.5 Source 27 – XRB

This source is now the source with the highest individual count rate in NGC 4449. Its luminosity has increased by nearly an order of magnitude since the *ROSAT* HRI observations of this galaxy in 1994, reported by Vogler & Pietsch (1997, see Table 4 for the comparative figures). This is confirmed by the results obtained by fitting it with a 5 keV thermal bremsstrahlung model, as used for the *ROSAT* data, where its luminosity is seen to have increased by a factor of at least 3. Its high luminosity and apparent long term variability would suggest that it is an high-mass X-ray binary (HMXB). The light curve shows no sign of variability within our 30 ks observation.

4 DIFFUSE EMISSION

A point source and background subtracted spectrum of the diffuse emission within the D_{25} ellipse was extracted and this is shown in Fig. 7. The fitted model shown is an absorbed 2 temperature fit ($\text{wabs}_{Gal}(\text{wabs}(\text{mekal}+\text{mekal}))$). The component due to Galactic absorption (wabs_{Gal}) has its absorption column density fixed at $N_H = 1.4 \times 10^{20} \text{ cm}^{-2}$ and the

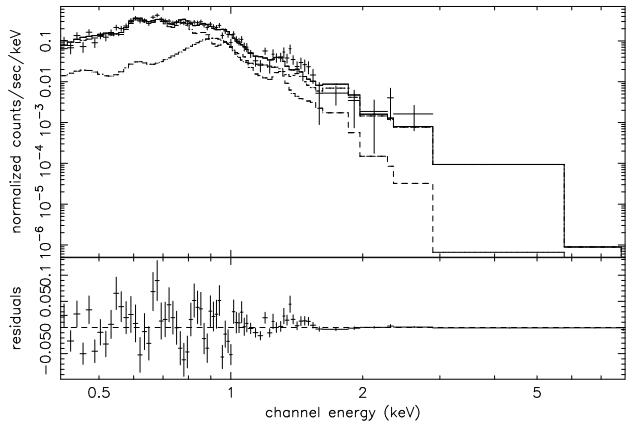


Figure 7. Fitted spectrum of the NGC 4449 diffuse emission. The fit shown is an absorbed two temperature fit, with a column density of $N_H = 1.4 \times 10^{20} \text{ cm}^{-2}$ assumed for Galactic absorption and fitted values of $N_H = (1.29 \pm 0.38) \times 10^{21} \text{ cm}^{-2}$ for the absorption within NGC 4449 and temperatures of (0.28 ± 0.01) and (0.86 ± 0.04) keV for the two thermal components. The fitted abundance for the two thermal components was found to be $(0.32 \pm 0.08)Z_\odot$

Table 5. Parameters for the two gas components of the diffuse emission. Assumptions: $V = 6 \times 10^{65} \text{ cm}^3$ (assumes spherical symmetry); $D = 2.93 \text{ Mpc}$; Filling factor, $f = 1$; $n_e \sim (EI/Vf)^{1/2}$ where EI is the emission integral ($\text{norm} \times 4\pi D^2$)/ 10^{-14} and norm is the normalization obtained from the spectral fitting; $P \sim 2n_e kT$, $M \sim n_e m_p V f$, $E_{Th} \sim 3n_e kTV$ and $t_{cool} \sim (3kT)/(\Lambda n_e)$ where $\Lambda = L_X/EI$.

Emission	Soft	Medium
kT (keV)	0.28 ± 0.01	0.86 ± 0.04
T (K)	$(3.24 \pm 0.12) \times 10^6$	$(9.97 \pm 0.46) \times 10^6$
L_X (erg s^{-1})	$(6.83^{+0.35}_{-0.36}) \times 10^{38}$	$(2.26^{+0.27}_{-0.26}) \times 10^{38}$
n_e (cm^{-3})	$0.0122^{+0.0003}_{-0.0003}$	$0.0059^{+0.0004}_{-0.0003}$
E_{Th} (erg)	$(9.66^{+0.43}_{-0.43}) \times 10^{54}$	$(1.49^{+0.12}_{-0.10}) \times 10^{55}$
M (M_\odot)	$(6.02^{+0.15}_{-0.15}) \times 10^6$	$(3.01^{+0.20}_{-0.15}) \times 10^6$
P (dyn cm^{-2})	$(1.07^{+0.05}_{-0.05}) \times 10^{-11}$	$(1.65^{+0.14}_{-0.11}) \times 10^{-11}$
t_{cool} (yr)	$(4.66^{+0.40}_{-0.41}) \times 10^8$	$(2.02^{+0.39}_{-0.36}) \times 10^9$

fit gives $N_H = (1.29 \pm 0.38) \times 10^{21} \text{ cm}^{-2}$ for the absorbing column local to NGC 4449 and values of kT of (0.28 ± 0.01) keV and (0.86 ± 0.04) keV for the soft and medium thermal components respectively. The fitted abundance for the two thermal components is $(0.32 \pm 0.08)Z_\odot$. The total absorption corrected flux in the 0.3 – 8.0 keV energy band for the diffuse emission is $(8.86^{+0.61}_{-0.60}) \times 10^{-13} \text{ erg s}^{-1} \text{ cm}^{-2}$, which corresponds to an absorption corrected luminosity of $(9.14^{+0.63}_{-0.62}) \times 10^{38} \text{ erg s}^{-1}$. Of this total emission, 75% is in the soft component and 25% in the medium component and allowance has been made for the flux lost during the point source subtraction. The errors shown here are based on the 90% confidence levels (1.64σ) for the normalization values obtained from the fit. Adding a power law component to allow for unresolved point sources within the diffuse emission neither improves the fit significantly nor alters the fitted parameters for the thermal components. The photon index resulting from such a fit was $\Gamma = 2.53$ and the frac-

tional split of the flux between the 3 components was: soft - $\sim 70\%$; medium - $\sim 25\%$; power law - $\sim 5\%$.

Other parameters of the two gas components have been calculated and these are shown in Table 5. The assumptions of spherical symmetry and a filling factor of 1 are both likely to be over estimates, particularly in the case of the medium emission (see below), resulting in the figures being under-estimates for n_e and P and over-estimates for M , E_{Th} and t_{cool} (see Strickland & Stevens 2000 for a discussion of filling factors and their likely values in galactic winds). These parameters will be discussed further in section 5.2.

In a further attempt to look at the abundances within the thermal components and in particular the ratio of α -elements to Fe the spectrum was re-fitted using variable abundance mekal models for the two thermal components. The abundances of the two thermal components were tied and the individual abundances of Mg, Ne, Si and Ca relative to Solar values were tied to that of O to form the group of α -elements. The fitted abundances for the α -elements and Fe were $(0.27^{+0.01}_{-0.03})Z_\odot$ and $(0.30^{+0.02}_{-0.02})Z_\odot$ respectively, with a $\chi^2/\text{d.o.f}$ of 201/117. The α/Fe ratio obtained from these values is not significantly different from solar ($(0.91^{+0.07}_{-0.10})Z_\odot$) in contrast to the values of Martin et al. (2002) for the dwarf starburst NGC 1569, where values of $2.1 - 3.9Z_\odot$ are quoted. The difference in these values could reflect different contributions made to the hot gas from SNe. Type II SNe are the sources of α - elements while Fe is produced from Type I SNe. The higher values for the α/Fe ratio for NGC 1569 would therefore suggest the presence of more Type II SNe than in NGC 4449 and could suggest that NGC 1569 is experiencing shorter more intense bursts of star-formation than NGC 4449. In the latter case, as discussed by Della Ceca et al., 1997, the star-formation and energy injection from star-forming regions may be more continuous as it is not clear that the present star-formation rate is much larger than that in the past on average and as such the longer time periods involved will reflect a larger contribution from Type I SNe.

In order to look for variations in temperature within the diffuse emission, the region it occupies was divided into 9 regions and the spectra for each region was extracted and fitted. The regions are shown overlaid on the smoothed (using a Gaussian with FWHM of 4 pixels $\sim 2''$), point source and background subtracted image of NGC 4449 in Fig. 8 and the resulting spectral fits are shown in Table 6. Where possible, a 2 temperature fit was used, but for the 4 regions with the lowest number of counts (1, 2, 3 and 7) this was not possible. Either the fitted temperatures of the 2 components were the same, within errors, or the normalization for one of the components went to zero. For these 4 regions, the results of single temperature fits are given. In addition, for each region, the $(m - s)/(m + s)$ hardness ratio has been calculated to further highlight variations within the galaxy and these are shown in Table 7. To make a comparison of the results contained in Tables 6 and 7 clearer, colour-coded maps of the temperatures, column densities and hardness ratios are shown in Fig. 10. The two upper panels compare the fitted temperatures for the 9 regions. The one on the left shows the temperatures of the softer thermal components, where two temperatures were fitted and the right panel shows the temperatures of the harder components. Where only one temperature was fitted, this is shown in both panels. The

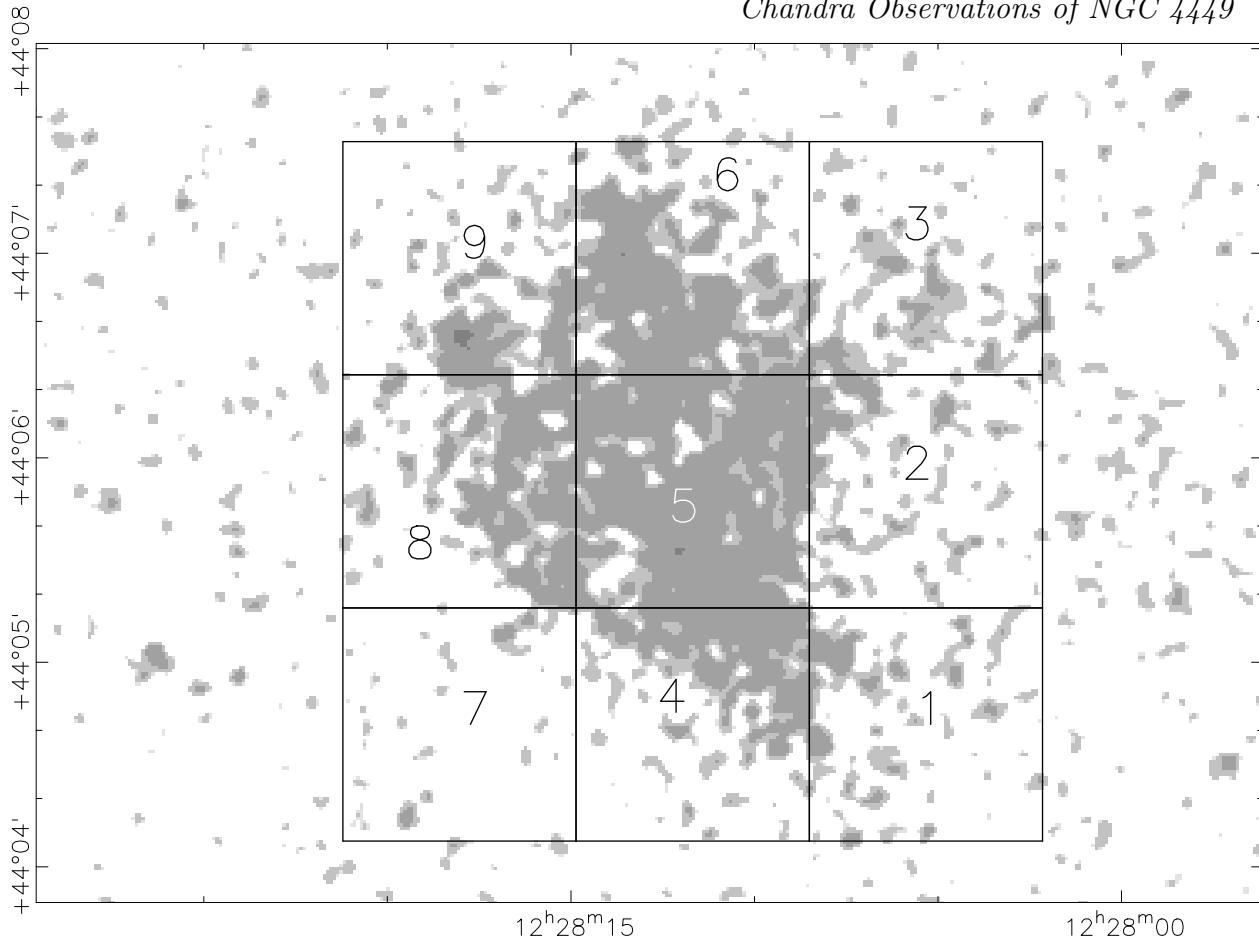


Figure 8. Low resolution (smoothed using a Gaussian with FWHM of 4 pixels $\sim 2''$) image of the point source and background subtracted diffuse X-ray emission overlaid with the 9 regions used to investigate the variation of temperature and absorbing column within the diffuse emission. The regions are identified by the overlaid numbers with region 1 in the SW corner and region 9 in the NE corner.

lower left panel compares the column densities ($\text{Log}(N_H)$) fitted to the 9 regions, while the lower right one shows how the $(m - s)/(m + s)$ hardness ratio varies.

These results are not very conclusive but do suggest a reduced column density in a region running from north to south across the centre of the galaxy and also across the northern edge and into the North-East of the galaxy. The temperature of the softer thermal components seem to be highest in the North of the galaxy and in an arc running south across the centre of the galaxy and into the South-East. The hardness ratios suggest that generally, the emission is slightly higher in the 0.3 – 0.8 keV energy band than in the 0.8 – 2.0 keV band. Looking at the soft, medium and hard energy band images (0.3 – 0.8 keV, 0.8 – 2.0 keV and 2.0 – 8.0 keV respectively), a difference can be seen between the spatial distribution of the extended diffuse emission in these 3 bands, (Fig. 9). These bands were originally chosen to have roughly equal counts in the 3 bands and they highlight the relative contributions made by the diffuse emission and point sources to the different bands. Surprisingly, the 0.3 – 0.8 keV band image shows the diffuse emission to be extending to the west of the galaxy into regions where the spectral fits gave some of the highest column densities. Such high absorption should reduce the soft thermal emission and suggests that the single temperature fits in these regions are not the best models. It is worth noting here that when two

temperature models were fitted to regions 1, 2 and 3, lower column densities were obtained but none of the results were well constrained.

To obtain a clearer picture of the distribution of peaks in the X-ray emission, surface brightness slices were taken across the galaxy in 4 directions (N to S, NW to SE, W to E and SW to NE), centred on the trough of the X-ray emission in the centre of the galaxy at $\alpha = 12^{\text{h}}28^{\text{m}}11.7^{\text{s}}$, $\delta = +44^{\circ}06'04.6''$ with a length of $200''$ and a width of $20''$. The positions of these slices are overlaid on the $\text{H}\alpha$ image of NGC 4449 (kindly supplied by Deidre A. Hunter) shown in Fig. 11. In addition surface brightness profiles were also taken from the $\text{H}\alpha$ image using the same slices. The resulting profiles from these slices are shown in Fig. 12, with those from the diffuse X-ray emission, shown by the crosses and dashed curves, overlaid on those from the $\text{H}\alpha$ emission (solid curves). Although the X-ray data has been point source subtracted, the $\text{H}\alpha$ data has not. There is very little correlation between the positions of the resolved X-ray point sources and the numerous HII regions seen in the $\text{H}\alpha$ data and so the slices are being used to look for association of the diffuse X-ray emission with the star-forming regions. See Section 5.1.2 for further discussion.

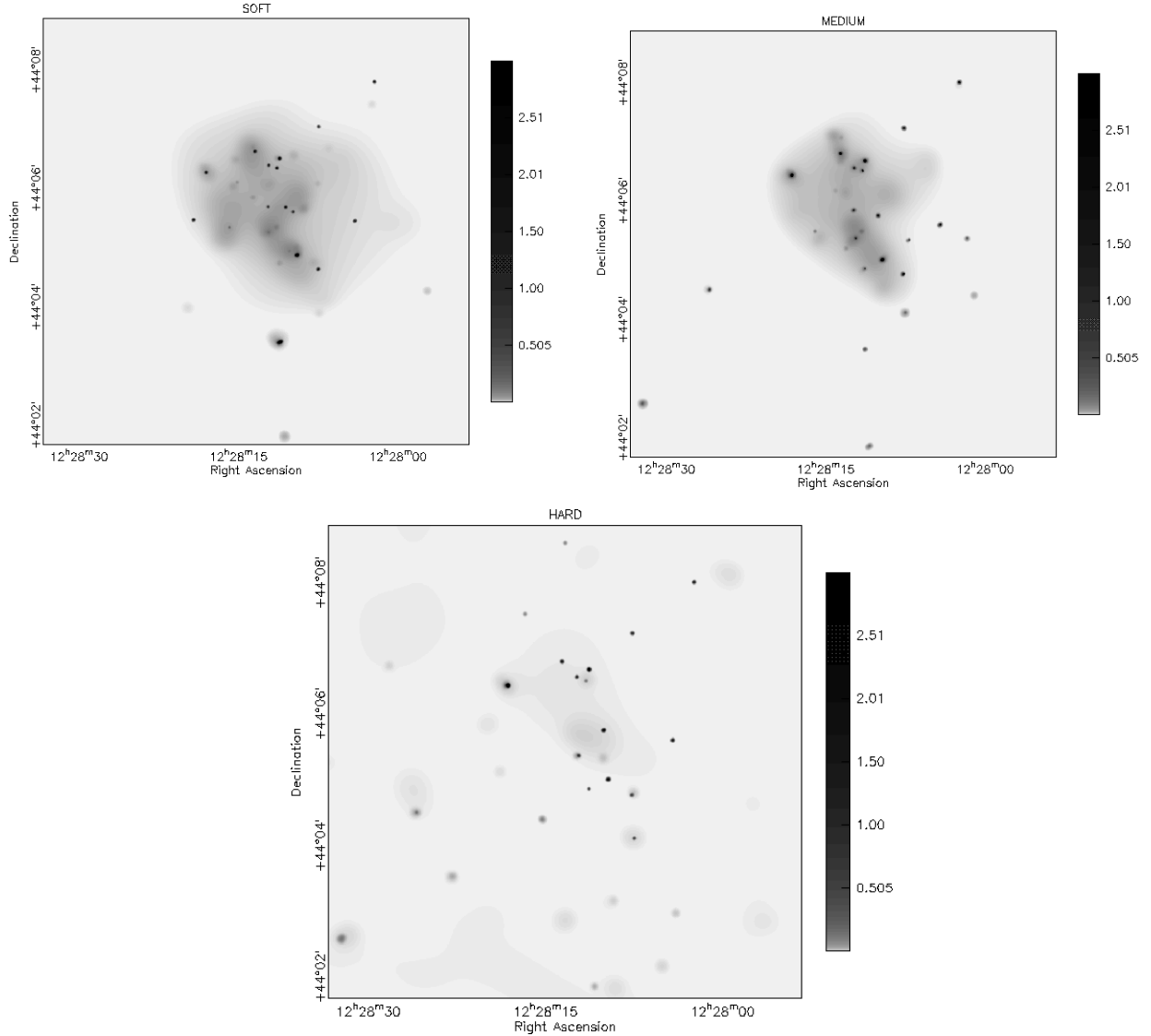


Figure 9. The 3 panels show smoothed images of the soft (0.3 – 0.8 keV), medium (0.8 – 2.0 keV) and hard (2.0 – 8.0 keV) energy bands, with the same grey-scale scaling, highlighting the differences in spatial distribution between the bands for the diffuse emission and the different spectral characteristics of the point sources.

5 DISCUSSION

It is apparent from Fig. 9 that the hardest (> 2 keV) fraction of the diffuse emission is confined to the central region of the galaxy along a ridge running from NNE to the centre. This is in the same direction as the orientation of the major axis of the galaxy. The medium (0.8 – 2.0 keV) diffuse emission is less extended than the soft (< 0.8 keV) emission with the most intense regions of emission in both these bands being coincident with the regions where the highest density of star clusters is seen (as identified by Gelatt et al. 2001), suggesting that this emission is associated with the increased star-formation occurring in these regions. The less intense bulging of the emission seen to the ESE and WNW could be indicative of a bipolar outflow along the minor axis of the galaxy as would be expected from standard superbubble models (Weaver et al. 1977). The higher column densities

seen in Table 6 and Fig 10 for the regions to the SE, SW and W of the galaxy would suggest that these areas lie behind more absorbing material present in the disk of the galaxy and that the eastern and northern edges of the galaxy are tilted towards us as shown in the cartoon representation of the galaxy’s morphology in Fig. 14. Allowing for NGC 4449’s position angle, this would mean the minor axis lies inclined to our line-of-sight (tilted both to the N and W) consistent with NGC 4449 being a Magellanic Irregular that is inclined at 56.2° to our line-of-sight. The lower column density of region 3, in particular, would suggest that the X-ray emission in that region comes from material lying above the galactic disk.

Table 6. Single or two temperature fits for the 9 regions of the diffuse emission (see text for further details). Columns 1 and 2 contain the region numbers and counts for each region respectively. Column 3 lists the column density for the absorbing gas within NGC 4449, column 4 the temperature(s) and column 5 the statistic for the fit for each region. Column 6 has the calculated absorption corrected luminosities for each of the regions, the errors shown are from the 90% confidence ranges (1.64σ) of the normalizations of the fits or are upper limits determined from these values where only one value is given. In all cases, the Galactic absorption column density was fixed at $N_H = 1.4 \times 10^{20} \text{ cm}^{-3}$.

Region	Counts	N_H (cm^{-2})	kT (keV)	$\chi^2/\text{d.o.f}$	L_X (erg s^{-1})
1	197 ± 21	2.87×10^{21}	0.19	17.9/14	$(2.29 \pm 0.34) \times 10^{38}$
2	246 ± 22	3.75×10^{21}	0.21	19.6/15	$(3.29 \pm 0.45) \times 10^{38}$
3	198 ± 21	4.38×10^{20}	0.45	22.7/14	$(3.52 \pm 0.70) \times 10^{37}$
4	440 ± 26	8.34×10^{20}	0.33, 1.03	36.3/20	$(1.09 \pm 0.27) \times 10^{38}$
5	1268 ± 39	1.28×10^{21}	0.27, 0.67	55.6/45	$(2.98 \pm 0.79) \times 10^{38}$
6	668 ± 30	1.08×10^{21}	0.39, 1.13	34.8/29	$(1.40 \pm 0.71) \times 10^{38}$
7	45 ± 17	4.69×10^{21}	0.27	4.20/7	$(5.44 \pm 47.29) \times 10^{37}$
8	442 ± 25	1.50×10^{21}	0.23, 0.58	19.5/20	$(1.33 \pm 0.40) \times 10^{38}$
9	294 ± 23	1.42×10^{21}	0.29, 1.93	11.96/17	$(8.94 \pm 2.68) \times 10^{37}$

Table 7. The $(m - s)/(m + s)$ hardness ratio for each of the 9 regions. Column 1 lists the region numbers as shown on Fig. 8, columns 2 and 3 contain the count rates in the soft and medium bands respectively and column 4 gives the calculated hardness ratios. The softer emission is shown by the regions with more negative values.

Region	Count rate in Soft band (counts/s^{-1})	Count rate in Medium band (counts/s^{-1})	$\frac{(m - s)}{(m + s)}$
1	$(5.33 \pm 0.57) \times 10^{-3}$	$(8.81 \pm 0.77) \times 10^{-3}$	0.246 ± 0.070
2	$(7.21 \pm 0.67) \times 10^{-3}$	$(2.78 \pm 0.49) \times 10^{-3}$	-0.443 ± 0.091
3	$(5.39 \pm 0.59) \times 10^{-3}$	$(3.26 \pm 0.51) \times 10^{-3}$	-0.246 ± 0.093
4	$(11.0 \pm 0.80) \times 10^{-3}$	$(7.81 \pm 0.70) \times 10^{-3}$	-0.170 ± 0.057
5	$(31.5 \pm 1.20) \times 10^{-3}$	$(22.4 \pm 1.10) \times 10^{-3}$	-0.169 ± 0.031
6	$(14.4 \pm 0.90) \times 10^{-3}$	$(13.9 \pm 0.90) \times 10^{-3}$	-0.018 ± 0.046
7	$(1.29 \pm 0.37) \times 10^{-3}$	$(0.01 \pm 0.38) \times 10^{-3}$	-0.985 ± 0.570
8	$(10.7 \pm 0.80) \times 10^{-3}$	$(7.23 \pm 0.67) \times 10^{-3}$	-0.194 ± 0.059
9	$(5.33 \pm 0.58) \times 10^{-3}$	$(6.43 \pm 0.64) \times 10^{-3}$	0.094 ± 0.074

5.1 Comparison with Observations at Other Wavelengths

5.1.1 Star Clusters

The galaxy contains many star clusters spread throughout the D_{25} ellipse and so star-formation is not confined to a single well-defined region within the galaxy. The highest density of star clusters identified by Gelatt et al. (2001) is coincident with the peak seen in the diffuse X-ray emission at $\alpha = 12^h 28^m 11.75^s$ and $\delta = +44^\circ 05' 36.1''$. (The largest of the contours labelled 3 in the lower panel of Fig. 13.) The peak in the diffuse emission to the SW of this at $\alpha = 12^h 28^m 09.65^s$ and $\delta = +44^\circ 05' 11.5''$ also has a large number of star clusters associated with it. It is likely that multiple superbubbles are being blown by the combined action of stellar winds and SN explosions from the individual stars within these star clusters, leading to the increased diffuse X-ray emission from hot, shock-heated gas in these regions. This is supported by the complex morphology seen in the patterns of peaks in the X-ray emission shown in Fig. 12.

5.1.2 Comparison with H α Emission

Fig. 13 shows X-ray contours overlaid on an H α map of NGC 4449 as well as the two separate images. This shows

that the X-ray and H α morphologies in the main body of the galaxy follow each other closely. The X-ray emission is also seen to extend out to the NW into what appears to be a hole in the H α emission, bounded by filaments, labelled F in the lower panel. This could be a wind-blown superbubble or the escape of hot gas from a ruptured bubble in the form of a super-wind, labelled SB/SW. Ultra-violet observations (Hill et al., 1998) have identified regions along the north-eastern edge of this hole which show sequential star-formation and this activity may be linked to the expansion of a super-bubble. As the bubble expands, it sweeps up and shock heats the ISM, leading to the formation of areas of increased density which can trigger star-formation. In addition, the observed filamentary structure seen in H α could be material from a ruptured bubble or entrained ISM material caught up in an outflow. A similar, if less pronounced effect also seems to be occurring to the SE, labelled SB. The extent of both emissions matches well, as can be seen by comparing the X-ray and H α surface brightness slices shown for the same regions in Fig. 12. The only exception seems to occur to the West of the galaxy where the diffuse X-ray emission appears to extend beyond the region of high H α intensity.

For the N to S and SW to NE slices, the overall profiles of the peaks are similar and they occupy a similar extent. The peaks of X-ray emission, in the northern half of these

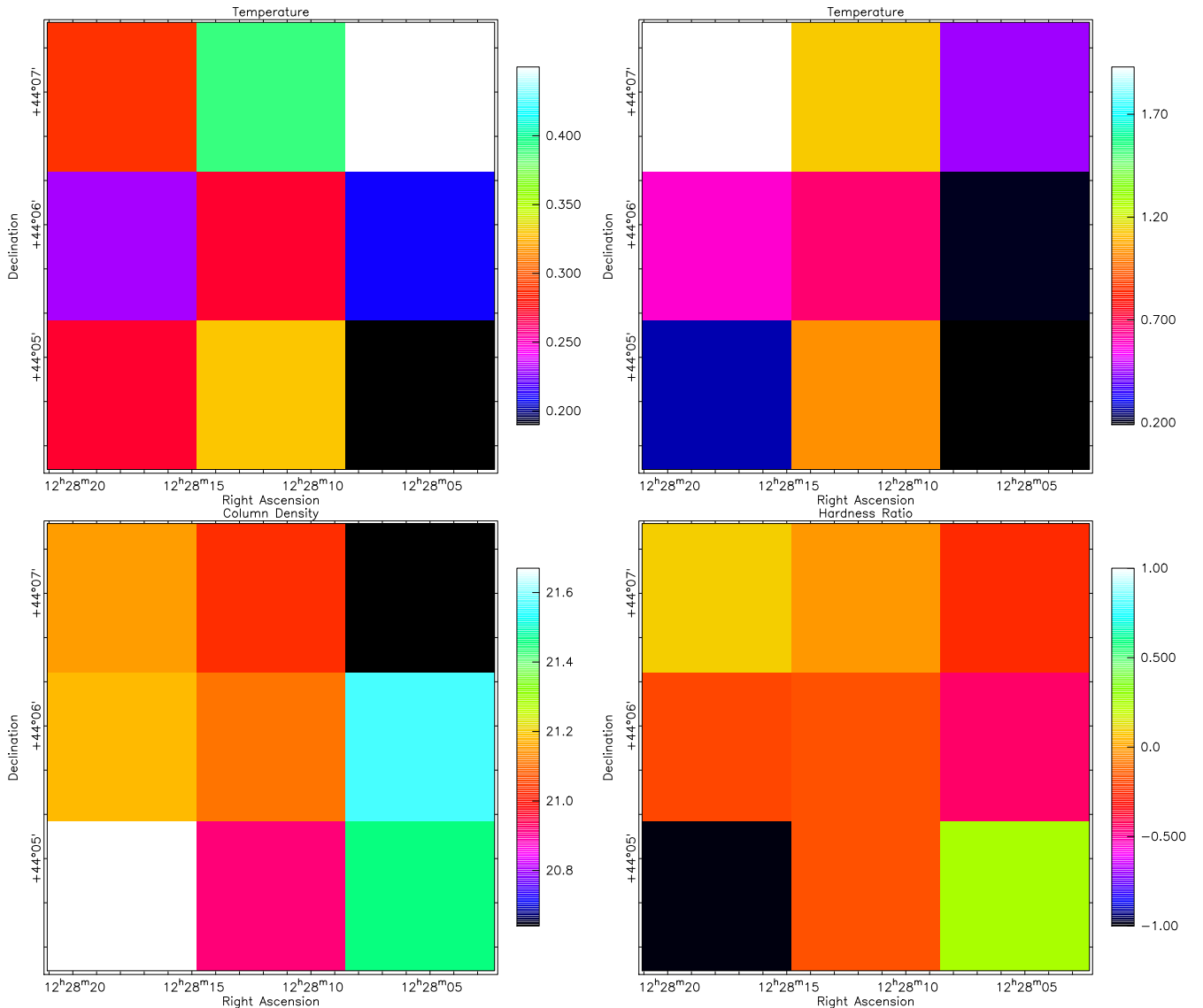


Figure 10. Colour-coded maps of the parameters investigated for variation within the diffuse emission. Top Left: The temperature, in keV, of the softer thermal component within the 9 regions. Top Right: The temperature, in keV, of the hotter thermal component, where two were fitted. For the four regions with one temperature fits (regions 1, 2, 3 and 7), the soft thermal component temperature is shown. Bottom Left: The logged value of the fitted column densities ($\text{Log}(N_H)$), in cm^{-2} , for the 9 regions. Bottom Right: The calculated $(m-s)/(m+s)$ hardness ratio for the 9 regions

slices, tend to fall inside the peaks of $\text{H}\alpha$ emission (i.e. they are slightly closer to the centre of the galaxy), with the intensity of the X-ray emission, in the N, being greatest close to the $\text{H}\alpha$ peaks. This is the type of behaviour discussed by Strickland et al. (2002) in model 5 of the connection between X-ray and $\text{H}\alpha$ emission, where the $\text{H}\alpha$ emission is attributed to a swept-up shell that has cooled, and surrounds a hot bubble of SN-ejecta. These potential bubbles in the N of the galaxy, labelled B in the lower panel of Fig. 13, have diameters ≤ 1 kpc and the most northern of the two does appear to be surrounded by an arc of increased intensity in the $\text{H}\alpha$ emission, most clearly visible in the upper left panel of Fig. 13. The increased intensity of the X-ray emission behind the $\text{H}\alpha$ peaks would be due to conductive evaporation of the swept-up material, which increases the density and

X-ray emissivity of the region where the hot gas and evaporated material mixes (Weaver et al. 1977). These two slices lie closest to the major axis of the galaxy and cut across the regions containing the highest densities of star clusters in the southern half of the galaxy. The association of the peaks is less clear on the south side of both of these slices and this may well be a result of the overlapping and merging of many wind-blown bubbles from the large number of star clusters found there.

The slices running from NW to SE and W to E lie closest to the minor axis of the galaxy and cut across the bulging of the diffuse X-ray emission. The slices show what appear to be cavities in the $\text{H}\alpha$ emission to both the NW and the E which are filled with X-ray emission, again suggesting the presence of wind-blown super-bubbles, while to the SE and

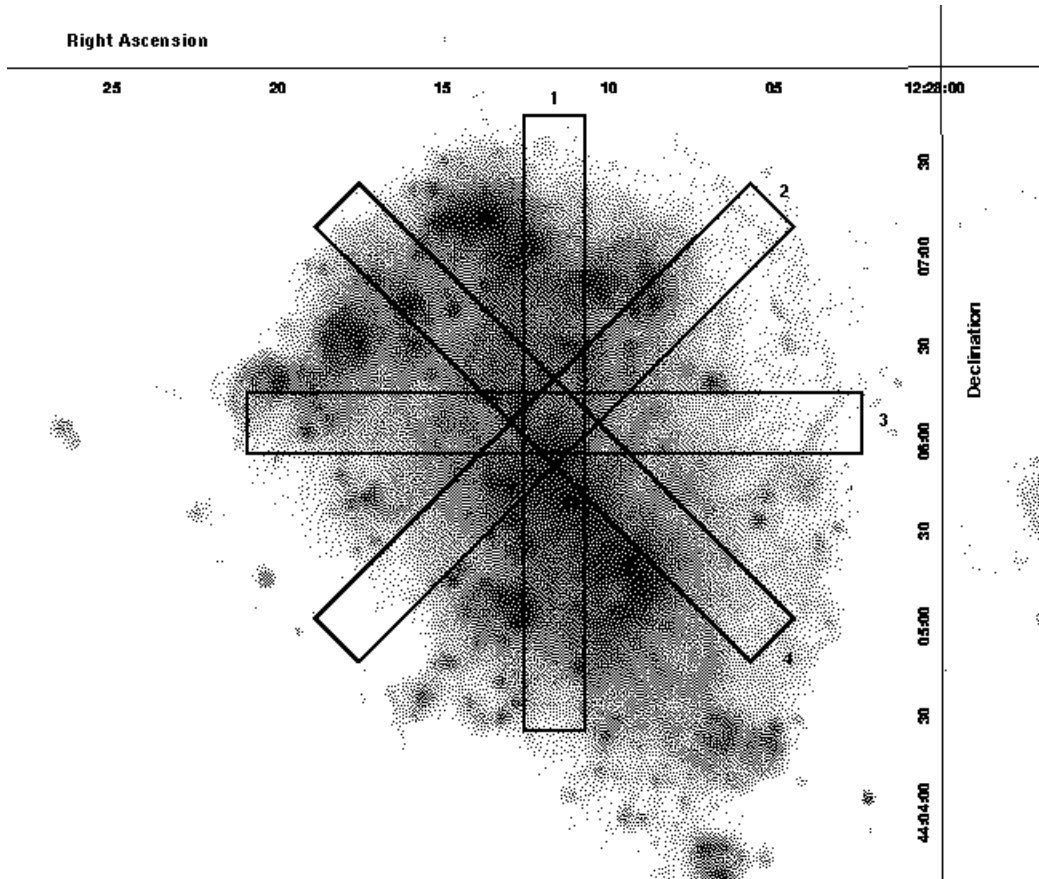


Figure 11. $H\alpha$ image of NGC 4449 with the positions of the four slices overlaid. Each slice is centred on $\alpha = 12^h28^m11.7^s$ and $\delta = +44^\circ06'04.7''$, has a length of $200''$ and a width of $20''$. Slice 1 runs from North to South, slice 2 from North-west to South-east, slice 3 from West to East and slice 4 from South-west to North-east. The resulting X-ray and $H\alpha$ profiles from these four slices are shown in Fig. 12.

W, the X-ray emission seems to lie outside the $H\alpha$ emission, more suggestive of ruptured super-bubbles, particularly to the west as seen by the distribution of X-ray contours, labelled 1, in the lower panel of Fig. 13.

5.1.3 The Large HI Halo and HI Clouds

The HI halo of NGC 4449 extends out to a radius of ~ 40 kpc (Bajaja et al. 1994) and its outer structure takes the form of enormous filaments and clouds (Hunter et al. 1998). The VLA observations of Hunter et al. (1998; 1999), show that the inner regions consist of a concentration of gas centred on the optical galaxy that takes the form of seven large HI complexes embedded in a lower density background, with the overall outline of the morphology bulging to the ESE and WNW as seen in the diffuse X-ray emission. Fig. 12 of Hunter et al. (1999), shows that the HI in the inner regions extends beyond the $H\alpha$ filament seen to the WNW in Fig. 13 and beyond the bulge in the diffuse X-ray emission to the ESE. This could be indicative of the swept up, compressed ambient interstellar medium lying outside the shells of two expanding super-bubbles. The regions of increased X-ray emission seen in the main body of the galaxy as well as lying close to regions of increased $H\alpha$ emission also occupy areas where three of the HI clouds lie. This is

suggestive of the increased HI density in these regions being caused by outflows from star clusters sweeping-up and compressing the ISM. The overall extent of the inner HI concentration is ~ 9 kpc and it is embedded in an elliptical region of lower concentration with a major axis of ~ 40 kpc from which streamers extend. By comparison, the extent of the diffuse X-ray emitting region is ~ 2.4 kpc along the major axis of the optical galaxy and ~ 1.6 kpc in an approximate ESE – WNW direction. The optical extent of the galaxy as measured by the D_{25} ellipse is ~ 4.35 kpc by ~ 3.35 kpc. Counter rotation is observed between the HI gas within the central region and that outside with the rotation velocity of the inner gas being ~ 18 km s $^{-1}$ and that of the streamers seen in the halo ~ 110 km s $^{-1}$. These two velocities and the distribution of the HI gas have implications for the potential of the hot gas, contained within any super-bubbles to escape. Modelling the potential of the galaxy as a simple spherically-symmetric, truncated, isothermal potential (Binney & Tremaine 1987) then the escape velocity at a distance r from the centre of the galaxy is given by:

$$v_{esc}(r) = 2^{1/2} v_{rot} [1 + \ln(r_t/r)]^{1/2} \text{ km s}^{-1} \quad (1)$$

where v_{rot} is the maximum rotation velocity of the galaxy in km s $^{-1}$ and r_t is the radius at which the potential is truncated. If the potential is truncated at the edge of the

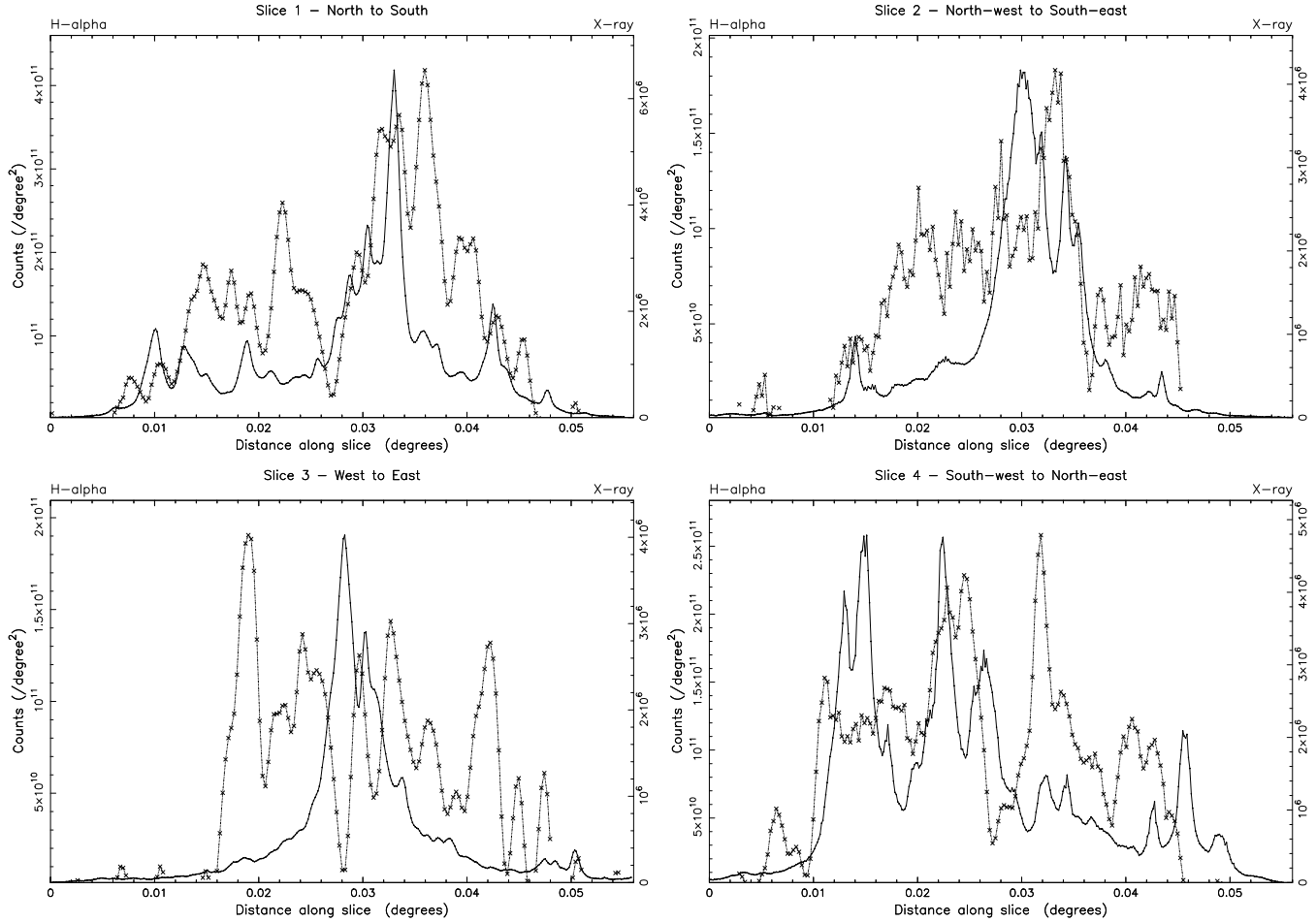


Figure 12. X-ray surface brightness slices (crosses and dashed curves) overlaid on the H α surface brightness slices (solid curves). The y-axes on the left of each panel gives the counts/degree² for the H α slices while the ones to the right are the values for the X-ray slices. Although these axes are on very different scales they do allow a comparison to be made of the spatial distribution of X-ray and H α peaks along each of the slices. All the slices are centred on $\alpha = 12^h 28^m 11.7^s$ and $\delta = +44^\circ 06' 04.7''$, located 0.028° along the slice, have a length of $200''$ and a width of $20''$. This position coincides with the central trough in the diffuse X-ray emission indicated by the small central contour labelled 2 at that position in Fig. 13.

inner HI concentration at $r_t \sim 4.5$ kpc then the escape velocity for the hot X-ray emitting gas at 1.6 kpc from the centre, assuming $v_{rot} \sim 18 \text{ km s}^{-1}$ would be $\sim 36 \text{ km s}^{-1}$. This is an upper limit as the value will decrease when the extent of the hot gas is deprojected. A similar calculation for the potential truncated at the edge of the HI halo at ~ 40 kpc, with $v_{rot} \sim 110 \text{ km s}^{-1}$ gives an upper value for $v_{esc} \sim 320 \text{ km s}^{-1}$. In the absence of radiative cooling, hot gas can escape the galaxy's potential if its temperature is greater than:

$$T_{esc} = 1.5 \times 10^5 (v_{100})^2 \text{ K} \quad (2)$$

where T_{esc} is the temperature required for the gas to exceed the galaxy's escape velocity and v_{100} is the escape velocity in units of 100 km s^{-1} (Martin 1999). The two escape velocities determined above have corresponding escape temperatures of $1.94 \times 10^4 \text{ K}$ and $1.54 \times 10^6 \text{ K}$ respectively. From the gas parameters given in Table 5 both the soft and medium components of the hot gas have temperatures in excess of these values. Eventual escape of the metal-enriched

SN ejecta contained within the super-bubbles seems possible for NGC 4449 but the distribution of the gas in the galaxy's extended halo could be as important as gravity in controlling whether the hot gas escapes or not. The presence of streamers of HI rather than an homogeneous distribution of material can facilitate the escape of hot gas through the gaps between the streamers.

5.1.4 Radio-X-ray Agreement

The 5 GHz VLA observation (Bignell & Seaquist 1983) identifies the known SNR (source 15) in NGC 4449 with the most intense peak of the radio emission. The next 3 most intense peaks on this radio observation also lie close to sources in our data (sources 10, 18 and 23) that have all been flagged as possible SNRs, although none convincingly. In addition, these radio peaks are coincident with the three brightest peaks of emission on the H α map, where intense star-formation is occurring and where the presence of SNRs in star clusters is to be expected.

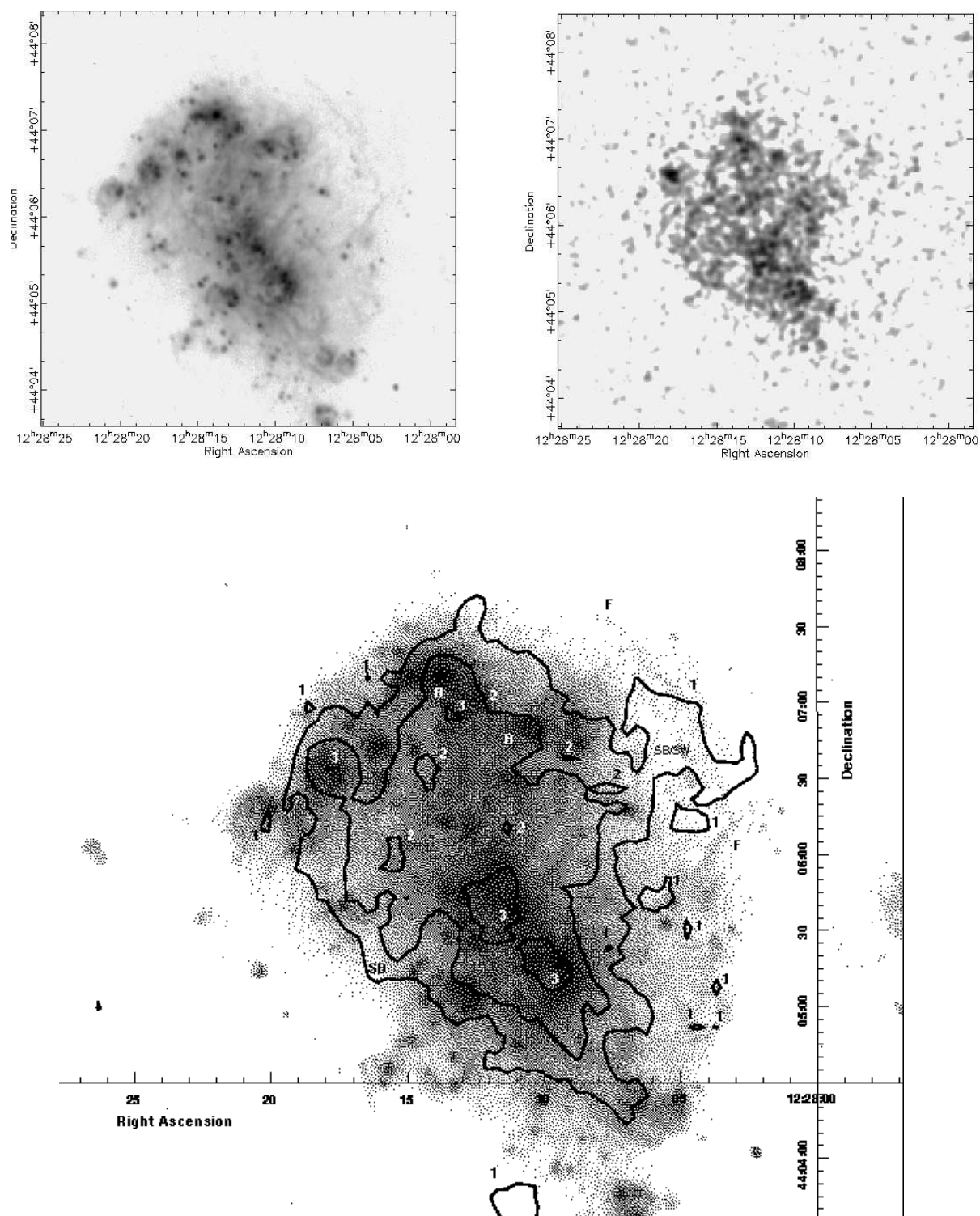


Figure 13. Top left: H α grey-scale image of NGC 4449. Top right: Point source and background subtracted diffuse X-ray grey-scale image of NGC 4449 on the same spatial scale as the H α image and with the same smoothing as in Fig. 8. Bottom: X-ray contours from the image shown top right overlaid on the H α image of NGC 4449. The X-ray contours labelled 1 are at a flux density of $0.65 \times 10^{-13} \text{ erg s}^{-1} \text{ cm}^{-2} \text{ arcmin}^{-2}$. Those labelled 2 are at a flux density of $1.3 \times 10^{-13} \text{ erg s}^{-1} \text{ cm}^{-2} \text{ arcmin}^{-2}$ and those labelled 3 are at $2.6 \times 10^{-13} \text{ erg s}^{-1} \text{ cm}^{-2} \text{ arcmin}^{-2}$. The background flux density level is $\sim 0.25 \times 10^{-13} \text{ erg s}^{-1} \text{ cm}^{-2} \text{ arcmin}^{-2}$. Also labelled are the filaments (F), bubbles (B), super-bubbles (SB) and super-wind (SW) discussed in the text.

5.2 Implications of the Calculated Gas Parameters on the Fate of NGC 4449

The presence of what appears to be a developing super-wind in this dwarf galaxy can have dramatic effects on its evolution. The lower gravitational potential of dwarfs makes the possibility of losing newly synthesized metals and swept-up ISM material more likely. As such it is worth considering the impact that the western super-bubble/super-wind might have on NGC 4449. The position of the super-bubble suggests that its origins may lie in 3 OB associations identified by Hill et al. (1994), that lie in the SW region of the main body of the galaxy where the highest density of star clusters is seen. The ages of these 3 OB associations were found to be, 5.9, 6.2 and 6.7 Myr while their corresponding masses were 1.6×10^5 , 6.3×10^5 and $2.5 \times 10^6 M_\odot$. The extent that the diffuse emission extends from the position of these OB associations is $\sim 1.7'$ or 1.4 kpc for our assumed distance down to a flux density level of $0.65 \times 10^{-13} \text{ erg s}^{-1} \text{ cm}^{-2} \text{ arcmin}^{-2}$. Assuming an average age for the OB associations of 6.3 Myr then to have travelled this distance the expansion velocity of the bubble has to be $\sim 220 \text{ km s}^{-1}$. This will be an underestimate since the deprojected distance will be greater than that assumed and also the presence of a density gradient in the halo above the disk of the galaxy will lead to acceleration of the super-wind. Further, from the calculated gas temperature of the soft component of the emission given in Table 5, a simple energy conservation analysis would give the average speed of a particle to be $\sim 280 \text{ km s}^{-1}$, which is in good agreement. At these sorts of velocities, it would take $\sim 200 \text{ Myr}$ for the super-wind to reach a distance of 40 kpc and so escape the HI halo. This is of the same order as the radiative cooling time for the soft component of the diffuse emission and again suggests that NGC 4449's huge HI halo may allow it to retain its newly synthesized metals and ISM. The likelihood that the HI halo will prevent blowout is also found when the criterion for blow-out defined by Mac Low & McCray (1988) is applied to NGC 4449. This is based on the parameter Λ , defined as the dimensionless rate of kinetic energy injection, given by:

$$\Lambda = 10^4 L_{mech,41} H_{kpc}^{-2} P_4^{-3/2} n_0^{1/2} \quad (3)$$

where $L_{mech,41}$ is the mechanical energy luminosity in units of $10^{41} \text{ erg s}^{-1}$, H_{kpc} is the galaxy scale-height in kpc, P_4 is the initial pressure of the ISM in units of $P/k = 10^4 \text{ K cm}^{-3}$ and n_0 its initial density. For blow-out to occur, the condition $\Lambda > 100$ has to be satisfied. For the whole of the X-ray emitting gas, the thermal energy content given in Table 5 is $2.46 \times 10^{55} \text{ erg}$. Assuming that this is the result of complete thermalization of the kinetic energy of the stellar-winds and SN ejecta, occurring over the lifetime of the OB associations, then L_{mech} for the whole galaxy is $\sim 1.2 \times 10^{41} \text{ erg s}^{-1}$ (a similar estimate to the $3 \times 10^{41} \text{ erg s}^{-1}$ obtained by Della Ceca et al, 1997, from the Leitherer & Heckman, 1995, starburst models). The actual thermalization will be less than complete, but as argued by Strickland & Stevens (2000), will most likely be between 10 and 100 %, meaning that the L_{mech} value above could be greater by up to an order of magnitude. Assuming the initial ISM pressure was similar to that of our Galaxy then $P_4 \sim 1$ and comparison to the gas pressures for the hot gas given in Table 5 show that they are an order of magnitude higher which is to be expected for an

adiabatically expanding over-pressured bubble. As a further assumption, the hot gas will be at a lower density than the initial ambient density of the ISM and an order of magnitude change will be assumed from the average value in Table 5. The result of using these figures in the above equation with $\Lambda = 100$ means that the scale-height for NGC 4449 has to be $\leq 9.5 \text{ kpc}$ which is somewhat less than the size of the HI halo. In addition this figure will be an overestimate since L_{mech} was estimated from the energy content of the whole volume assumed to be occupied by the diffuse emission. The volume of the western superbubble is only $\sim 10\%$ of the total volume and if the ambient ISM density is assumed to be closer to that of the hot gas then again the scale-height will decrease. If the halo has holes in it, as suggested by the presence of streamers rather than an homogeneous distribution, then escape is more likely.

If escape occurs then the amount of mass lost may affect NGC 4449's ability to continue star-formation. Assuming the super-bubble has around a tenth of the volume of the diffuse emission and as such around a tenth of the mass given in Table 5 then over 6.3 Myr, the average mass injection rate will have been $0.14 M_\odot \text{ yr}^{-1}$, a figure which is similar to that predicted for Mrk 33 (Summers et al. 2001), another dwarf galaxy that may be developing a super-wind. If this rate of mass injection was maintained while the super-bubble/super-wind expanded to the edge of the HI halo over a time-span of $\sim 200 \text{ Myr}$ then the total amount of mass it would contain would be $\sim 2.5 \times 10^7 M_\odot$. This value is greater than the mass contained within the 3 OB associations ($\sim 3.3 \times 10^6 M_\odot$) and the time-scale is also in excess of the life-times of the massive stars found there, so unless a large amount of mass-loading from ISM material is to occur this would be an over-estimate of the mass that the super-bubble/super-wind would contain on escape. Compared to the total mass of NGC 4449 of $\sim 4 \times 10^{10} M_\odot$ this is only about 0.1% of the galaxy's total mass. As the time-scale required is in excess of the life-times of the massive stars then the energy-injection rate would also decrease before escape was attained, suggesting that the bubble expansion is likely to stall. Hence it seems unlikely that the development of this super-bubble/super-wind in NGC 4449 will have a great deal of effect on the galaxy's ability to both retain its products of star-formation and continue star-formation in the future.

5.3 Morphology of NGC 4449

Fig. 14 shows a cartoon of the possible morphology of NGC 4449 and in particular shows how the diffuse X-ray, H α and HI emissions may be associated with each other, at the maximum extent of the X-ray and H α emission, if the galaxy is assumed to have a bi-polar outflow in the form of two wind-blown super-bubbles along its minor axis. The stars represent the approximate positions of the starclusters in the two densest populated regions, as identified by Gelatt et al. (2001). The structure shown in the X-ray emission in the NW super-bubble may be indicative of the bubble rupturing and X-ray emission beginning to extend beyond the H α emission as is suggested in the X-ray and H α slices of Fig. 12. A comparison of the NW-SE and W-E slices which run along the northern and southern edges of the bubble respectively suggest that the X-ray emission is bounded by the H α emission to the north but not to the South. A similar

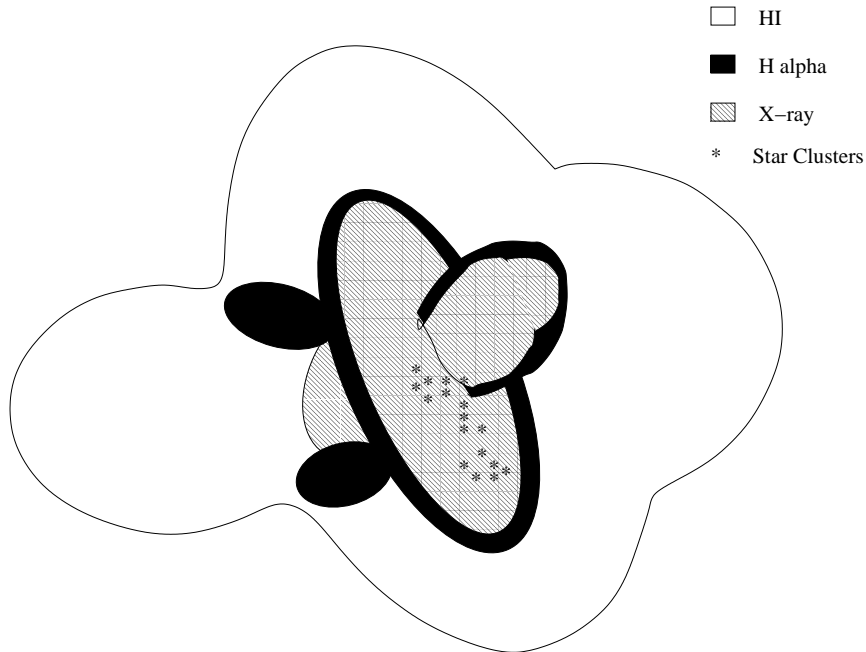


Figure 14. Cartoon representation of the relationship between the X-ray, $H\alpha$ and HI morphologies of NGC 4449 and the approximate positions of the starclusters in the densest groups (from Gelatt et al. 2001). The extent of the X-ray and $H\alpha$ emissions were determined from a comparison of matched images of the X-ray data and the $H\alpha$ image. The extent of the HI shown is estimated from Fig. 12 of Hunter et al. (1998) which shows HI contours overlaid on an image of the same $H\alpha$ data. The structure shown in the X-ray bubble to the NW represents the extension of the X-ray emission seen in this direction in Fig. 13 that may actually extend beyond the $H\alpha$ filament seen there and as such may be indicative of the escape of hot gas from a ruptured super-bubble in the form of a super-wind.

picture is seen to the East of the galaxy where the emission to the East seems to be bounded whilst that to the SE is unbounded. In the regions of intense star-formation to the S, there are several peaks of emission in both the X-ray and $H\alpha$, indicative of a confused morphology where the presence of several wind-blown bubbles is to be expected and their overlapping both physically and in projection will make individual bubbles impossible to identify. To the N, the presence of 2 bubbles with diameters ≤ 1 kpc seems to be indicated in the surface brightness slices of Fig. 12. The HI outline on Fig. 14 represents the extent of the inner HI cloud complexes and HI ISM down to a column density of $15 \times 10^{20} \text{ cm}^{-2}$ as shown on Figs. 10 and 12 of Hunter et al. (1999). Comparing these two figures with Fig. 13 above, although obviously different in size, all three types of emission do appear to have a similar outline to their morphologies.

6 SUMMARY AND CONCLUSIONS.

In summary, we have presented an analysis of the X-ray data obtained from a 30 ks observation, of the Magellanic Irregular, starburst galaxy NGC 4449, by the *CHANDRA* satellite. We find X-ray emission from 32 discrete point sources in the S3 chip data with 24 of them lying within the optical extent of the galaxy, as measured by the extent of the D_{25} ellipse. Some of these can be clearly identified as SNRs, others as XRBs and there are also several SSS. We calculate an age for the previously identified SNR (source 15) of

270 yr and a density for the medium into which it has exploded of being $\leq 200 \text{ cm}^{-3}$. The bright SSS (source 14) is a candidate for being a white dwarf binary system, while the source exhibiting the highest count rate during the observation (source 27), shows long term variability and is most likely an HMXB.

The galaxy has a very extended distribution of HI, but the inner concentration of HI has an overall general morphology which also follows that of the X-ray emission but on a larger scale. The HI complexes within the inner region could be the result of outflows from the multiple star clusters in the starburst of NGC 4449 compressing and driving the ambient ISM of the galaxy away from the centre, both along the minor axis of the galaxy and above regions of increased star formation within the disk. The overall extent of the inner HI concentration is ~ 9 kpc, that of $H\alpha$ is $\sim 4.35 \times 3.35$ kpc and that of the X-ray emission is $\sim 2.5 \times 1.6$ kpc., with this central region being embedded within an huge HI halo extending out to ~ 40 kpc.

The total X-ray luminosity of NGC 4449 in the 0.3 – 8.0 keV energy band is $(2.46 \pm_{0.20}^{0.19}) \times 10^{39} \text{ erg s}^{-1} \text{ cm}^{-2}$. Of this, $\sim 60\%$ is due to resolved point sources and the rest is due to diffuse X-ray emission. As suggested by this analysis and those of other starburst galaxies (e.g. NGC 253, Strickland et al. 2002; NGC 1569, Martin et al. 2002, Della-Ceca et al. 1996; NGC 4449 Della Ceca et al. 1997), the diffuse X-ray emission is emerging as a multi-phase environment requiring complex spectral models which the

spectral resolution of even current X-ray telescopes cannot meaningfully constrain. We thus conclude that the diffuse X-ray emission contains gas at, at least two different temperatures and evidence for unresolved point sources. The fitted gas temperatures are (0.28 ± 0.01) keV and (0.86 ± 0.04) keV for the soft and medium components respectively and their respective absorption corrected fluxes in the 0.3–8.0 keV band are $(6.66 \pm_{0.35}^{0.34}) \times 10^{-13}$ erg s $^{-1}$ cm $^{-2}$ and $(2.20 \pm_{0.25}^{0.26}) \times 10^{-13}$ erg s $^{-1}$ cm $^{-2}$ corresponding to luminosities of $(6.83 \pm_{0.36}^{0.35}) \times 10^{38}$ erg s $^{-1}$ and $(2.26 \pm_{0.26}^{0.27}) \times 10^{38}$ erg s $^{-1}$. This diffuse emission seems to be more heavily absorbed in the SW of the galaxy and shows a higher temperature in the central and eastern regions consistent with NGC 4449 being an inclined Magellanic Irregular galaxy, with its minor axis inclined to the N and W of our line-of-sight. The morphologies of the X-ray and H α emissions from the galaxy follow each other closely and the X-ray emission appears to fill cavities in the H α emission to the NW and E – highly suggestive of wind-blown super-bubbles extending along the minor axis of the galaxy. To the SE and W, the X-ray emission seems to lie outside the H α emission and this may indicate the developing of a super-wind from the rupture of the super-bubbles. The large number of peaks in emission seen in both the H α and diffuse X-ray data indicates a complex morphology within the main body of the galaxy. Regions containing small, (≤ 1 kpc), bubbles of X-ray emission surrounded by shells of H α emission are seen, that are produced by the combined action of stellar-winds and SN explosions from massive stars, shock-heating both the stellar-ejecta and ISM and sweeping it into shells as the ejecta drives its way out of star clusters.

The hot X-ray emitting gas has a total thermal energy content of $\sim 2.5 \times 10^{55}$ erg and a total mass of $\sim 9.0 \times 10^6 M_{\odot}$. The super-bubble/super-wind extending to the WNW of the galaxy occupies around 10% of the total volume occupied by the hot gas (assuming a filling factor of 1). The origin of this out-flow appears to be the concentration of star clusters observed in the SW region of the galaxy disk (Hill et al. 1994). At present, the average energy injection rate for the whole galaxy is $\sim 1.2 \times 10^{41}$ erg s $^{-1}$ and the mass injection rate into the super-bubble is $\sim 0.14 M_{\odot}$ yr $^{-1}$. It seems unlikely that this bubble can escape from the huge HI halo at its current estimated expansion speed of ~ 220 km s $^{-1}$, as the time required is in excess of the lifetimes of the massive stars of the star clusters and comparable to the radiative cooling time of the soft component of the diffuse emission, whilst the expansion velocity is less than the estimated escape velocity from the HI halo. However, the current temperatures of both gas components imply that they are capable of escaping the galaxy’s gravitational potential and so venting metal-enriched, hot gas into the IGM. The crucial factors are the time for which energy injection can be maintained and the actual distribution of HI in the halo of NGC 4449. The less homogeneous the distribution, the more likely the possibility that some of the hot gas can escape. At current mass injection rates, the total mass loss would be $< 1\%$ of the galaxy’s mass and as such would not have a catastrophic effect on NGC 4449.

ACKNOWLEDGEMENTS

LKS and IRS acknowledge funding from a PPARC studentship and Advanced Fellowship respectively. DKS is supported by NASA through *CHANDRA* Postdoctoral Fellowship Award Number PF0-10012, issued by the *CHANDRA* X-ray Observatory Center, which is operated by the Smithsonian Astrophysical Observatory for and on behalf of NASA under contract NAS8-39073. Our thanks go to Deidre A. Hunter for kindly providing us with the H α image of NGC 4449.

REFERENCES

- Aaronson M., Mould J., 1983, ApJ, 265, 1
 Bajaja E., Huchtmeier W. K., Klein U., 1994, A&A, 285, 385
 Balick B., Heckman T., 1978, ApJ, 226, L7
 Bignell R. C., Seaquist E. R. 1983, ApJ, 270, 140
 Binney J., Tremaine S., 1987, Galactic Dynamics. Princeton Univ. Press, Princeton
 Blair W. P., Kirshner R. P. Winkler Jr. P. F., 1983, ApJ, 272, 84
 Blair W. P., Raymond J. C., Fesen R. A. Gull T. R., 1984, ApJ, 279, 708
 Böker T., van der Marel R. P., Mazzuca L., Rix H-W., Rudnick G., Ho L. C., Shields J. C., 2001, AJ, 121, 1473
 Bothun G. D., 1986, AJ, 91, 507
 Brandt W. N., Alexander D. M., Hornschemeier A. E., Garmire G. P., Schneider D. P., Barger A. J., Bauer F. E., Broos P. S., Cowie L. L., Townsley L. K., Burrows D. N., Chartas G., Feigelson E. D., Griffiths R. E., Nousek J. A., Sargent W. L. W., 2001, AJ, 122, 2810
 Della Ceca R., Griffiths R. E., Heckman T. E., MacKenty J. W., 1996 ApJ, 469, 662
 Della Ceca R., Griffiths R. E., Heckman T. E., 1997, ApJ, 485, 581
 de Vaucouleurs G., de Vaucouleurs A., Corwin J. R., Buta R. J., Paturel G., Fouque P., 1991, Third Reference Catalogue of Bright Galaxies, Version 3.9. University of Texas Press, Austin
 Ebisawa K., Mukai K., Kotani T., Asai K., Dotani T., Nagase F., Hartmann H. W., Heise J., Kahabka P., van Teeseling A., 2001, ApJ, 550, 1007
 Gelatt A. E., Hunter D. A., Gallagher J. S., 2001, PASP, 113, 142
 Hartmann L. W., Geller M. J., Huchra J. P., 1986, AJ, 92, 1278
 Hill R. S., Home A. T., Smith A. M., Bruhweiler F. C., Cheng K-P., Hintzen P. M. N., Oliverson R. J., 1994, ApJ, 430, 568
 Hill R. S., Fanelli M. N., Smith D. A., Bohlin R. C., Neff S. G., O’Connell R. W., Roberts M. S., Smith A. M., Stecher T. P., 1998, ApJ, 507, 179
 Hunter D. A., Gallagher J. S., 1990, ApJ, 362, 480
 Hunter D. A., Gallagher J. S., 1997, ApJ, 475, 65
 Hunter D. A., Thronson Jr. H. A., 1996, ApJ, 461, 202
 Hunter D. A., Wilcots E. M., van Woerden H., Gallagher J. S., Kohle S., 1998, ApJ, 495, L47
 Hunter D. A., van Woerden H., Gallagher J. S., 1999, AJ, 118, 2184
 Karachentsev I. D., Drozdovsky I. O., 1998, A&AS, 131, 1
 Klein U., Hummel E., Bomans D. J., Hopp U., 1996, A&A, 313, 396
 Leitherer C., Heckman T. M., 1995, ApJS, 96, 9
 Mac Low M-M. McCray R., 1988, ApJ. 324, 776
 Martin C. L., 1997, ApJ, 491, 561
 Martin C. L., 1999, ApJ, 513, 156
 Martin C. L., Koblunicky H.A., Heckman T. M., 2002, ApJ, 574, 663

- Patnaude D. J., Fesen R. A., 2003, Submitted to ApJ, astro-ph/0212409
- Seaquist E. R., Bignell R. C., 1978, ApJ, 226, L5
- Strickland D. K., Heckman T. M., Weaver K. A., Dahlem M., 2000, AJ, 120, 2965
- Strickland D. K., Heckman T. M., Weaver K. A., Hoopes C. G., Dahlem M., 2002, ApJ, 568, 689
- Strickland D. K., Stevens I. R., 2000, MNRAS, 314, 511
- Summers L. K., Stevens I. R., Strickland D. K., 2001, MNRAS, 327, 385
- Thronson Jr. H. A., Hunter D. A., Telesco C. M., Harper D. A., Decher R., 1987, ApJ, 317 180
- Vogler A., Pietsch W., 1997, A&A, 319, 459
- Weaver K. A., 2001, in *The Central kpc of Starbursts and AGN: The La Palma Connection. ASP Conference Proceedings*, Vol 249, 389, Eds. J. H. Knapen, J. E. Beckman, I. Sholsman, T. J. Mahoney, San Francisco, ASP
- Weaver R., McCray R., Castor J., Shapiro P., Moore R., 1977, ApJ, 218, 377
- Yokogawa J., Imanishi K., Koyama K., Nishiuchi M., Mizuno M., 2002, PASJ, 54, 53
- Zezas A., Fabbiano G., Prestwich A., Ward M., Murray S., 2001, in *The Central kpc of Starbursts and AGN: The La Palma Connection. ASP Conference Proceedings*, Vol 249, 425, Eds. J. H. Knapen, J. E. Beckman, I. Sholsman, T. J. Mahoney, San Francisco, ASP